

Spectrophotometric templates for core-collapse supernovae and their application in simulations of time-domain surveys

M. Vincenzi^{1,2★}, M. Sullivan³, R. E. Firth³, C. P. Gutiérrez³, C. Frohmaier¹,
M. Smith³, C. Angus³ and R. C. Nichol¹

¹*Institute of Cosmology and Gravitation, University of Portsmouth, Portsmouth PO1 3FX, UK*

²*DISCnet Centre for Doctoral Training, University of Portsmouth, Portsmouth PO1 3FX, UK*

³*School of Physics and Astronomy, University of Southampton, Southampton SO17 1BJ, UK*

Accepted 2019 August 14. Received 2019 August 13; in original form 2019 June 6

ABSTRACT

The design and analysis of time-domain sky surveys require the ability to simulate accurately realistic populations of core-collapse supernova (SN) events. We present a set of spectral time-series templates designed for this purpose, for both hydrogen-rich (Type II, IIn, and IIB) and stripped-envelope (Type Ib, Ic, and Ic-BL) core-collapse SNe. We use photometric and spectroscopic data for 67 core-collapse SNe from the literature, and for each generate a time-series spectral template. The techniques used to build the templates are fully data driven with no assumption of any parametric form or model for the light curves. The template-building code is open source, and can be applied to any transient for which well-sampled multiband photometry and multiple spectroscopic observations are available. We extend these spectral templates into the near-ultraviolet to $\lambda \simeq 1600$ Å using observer-frame ultraviolet photometry. We also provide a set of templates corrected for host galaxy dust extinction, and provide a set of luminosity functions that can be used with our spectral templates in simulations. We give an example of how these templates can be used by integrating them within the popular SN simulation package SNANA, and simulating core-collapse SNe in photometrically selected cosmological Type Ia SN samples, prone to contamination from core-collapse events.

Key words: methods: data analysis – methods: statistical – supernovae: general.

1 INTRODUCTION

Current and future time-domain optical surveys are expected to discover many thousands of optical transients and supernovae (SNe) on a nightly basis. This number far surpasses the resources available to spectroscopically confirm the nature of each detected event, and thus new approaches must be developed in order to exploit these samples. Techniques to model the composition of transients in future data sets are needed to guide and prioritize the limited follow-up resources, methods to classify transients based on their (possibly incomplete) photometric light curves are required to identify events of interest for different science goals, and accurate models of the expected contamination from core-collapse SNe are needed for future cosmological samples of Type Ia SNe (SNe Ia).

Each of these tasks requires the ability to accurately model populations of core-collapse SNe. For example, SN photometric classification techniques critically rely on templates of core-collapse SNe, whether these are classical ‘template-fitting’ techniques (e.g. Kuznetsova & Connolly 2007; Sako et al. 2008, 2011; Rodney & Tonry 2009; Gong, Cooray & Chen 2010), or whether these are

machine learning techniques (Ishida & de Souza 2013; Karpenka, Feroz & Hobson 2013; Lochner et al. 2016; Möller & de Boissière 2019) that must be trained on representative samples of data, often based on simulations.

A similar argument can be extended to SN Ia photometric cosmological analyses. The potential of cosmological analyses using photometrically classified SNe Ia is significant and robust techniques will be required to unlock the power of future samples. In current SN Ia photometric cosmological analyses, the effect of contamination is assessed using simulation techniques (Kunz, Bassett & Hlozek 2007; Hlozek et al. 2012; Kessler & Scolnic 2017), which are sensitive to how well the contamination can be modelled, rather than to the classification techniques used. The recent analysis of the photometric SN Ia sample from the Panoramic Survey Telescope and Rapid Response System (Pan-STARRS 1 (PS1); Jones et al. 2017, 2018) has shown that simulations of core-collapse SNe using currently available template libraries and luminosity functions (LFs) significantly underestimate the apparent core-collapse SN contamination in the data, and a significant tuning of the underlying properties of the core-collapse SN population is required.

Historically, SN spectral templates have been constructed by combining together multiple observations of different SNe of

* E-mail: maria.vincenzi@port.ac.uk

the same type into some representative average spectral series of the class, interpolating between data to produce a spectral series sampled perhaps daily. This is particularly applicable to SNe Ia (Leibundgut et al. 1991; Nugent, Kim & Perlmutter 2002; Hsiao et al. 2007), where the object-to-object diversity is relatively limited and quantifiable, and the concept of an average spectrum is straightforward. The advantage of this approach is that a spectrum can be interpolated on any epoch, from which photometry can be synthesized. However, this method is not as suitable for the far more heterogeneous core-collapse SNe, where the spectral diversity is larger and the observed data typically sparser, thus making it more difficult (and perhaps conceptually meaningless) to combine data from different events into a single template.

This is well demonstrated by the complex classification scheme for core-collapse SNe that depends on their spectral (e.g. Filippenko 1997) and sometimes photometric (e.g. Barbon, Ciatti & Rosino 1979; Patat et al. 1994; Arcavi et al. 2012) properties; for a recent review, see Gal-Yam (2017). Type II SNe (SNe II) have clear signatures of hydrogen in their spectra, whereas Type I SNe do not; Type Ib SNe (SNe Ib) have helium absorption lines, whereas Type Ic SNe (SNe Ic) do not; and neither SNe Ib nor SNe Ic have the strong silicon or sulphur lines usually present in thermonuclear explosions. SNe Ic are often further divided according to whether they have broad lines (BLs) in their spectra, indicating very high velocities in the expanding ejecta. Type IIb SNe (SNe IIb; Filippenko, Matheson & Ho 1993) are transition objects that begin as SNe II, but lose the hydrogen and develop increasingly strong helium lines as they evolve. Type IIn SNe (SNe IIn; Schlegel 1990) are SNe II that present narrow hydrogen emission lines, interpreted as the result of interactions between SN ejecta with circumstellar material (Chugai 1990; Smith et al. 2008). Thus, for core-collapse SNe, a library of spectral templates, rather than a single average template, is more appropriate.

The first library of core-collapse SN templates was developed for the Supernova Photometric Classification Challenge (SNPhotCC; Kessler et al. 2010a,b), with 41 templates based on multiband light curves of spectroscopically confirmed core-collapse SNe from the Carnegie Supernova Project, the Supernova Legacy Survey, and the Sloan Digital Sky Survey-II (SDSS-II). In the absence of high-cadence spectral time series for these events, the same spectral energy distribution (SED) time series was used for each event, taken from the popular templates of Peter Nugent,¹ and matched to the observed photometry of each individual event. Ultraviolet (UV) and near-infrared (near-IR) wavelengths for these templates are poorly constrained, and only observer-frame U/u -band photometry is included. This original library has been improved with additional events and is also used in the Photometric LSST Astronomical Time-Series Classification Challenge (The PLAsTiCC team et al. 2018).

Since the SNPhotCC challenge, the number of published core-collapse SNe has significantly increased, with the release of large samples of spectroscopic (Modjaz et al. 2014; Hicken et al. 2017; Stritzinger et al. 2018a; Shivvers et al. 2019) and photometric (Arcavi et al. 2012; Taddia et al. 2013; Bianco et al. 2014; Gutiérrez et al. 2017a,b; Hicken et al. 2017; Stritzinger et al. 2018a; Taddia et al. 2018) data, alongside many single object studies of interesting or unusual events (e.g. Pignata et al. 2011; Arcavi et al. 2017a; Terreran et al. 2017; Anderson et al. 2018; Bersten et al. 2018; Izzo et al. 2019). UV coverage of core-collapse SNe has also

improved, with observations from the *Swift* satellite using the Ultraviolet/Optical Telescope (UVOT) instrument (Román et al. 2005; Bufano et al. 2009; Brown et al. 2014; Brown, Román & Milne 2015), and follow-up programs using the *Hubble Space Telescope* and *GALEX* (e.g. Gal-Yam et al. 2008; Ben-Ami et al. 2012, 2015). The construction of templates in the UV is essential for simulating transients at higher redshift, where the rest-frame UV is redshifted into the observer-frame optical.

Taking advantage of these new data, in this paper we present a method to construct a SN spectral template based on individual SN events for which well-constrained multiband light curves and sparse spectroscopic observations have been measured. This technique is data driven, and in principle can be generalized to any type of transient. Each final spectral template generated by our method consists of a daily sampled spectral time series, extended into the UV, and optionally corrected for extinction due to dust in the SN host galaxy. Our goal is then to apply this general technique to all suitable core-collapse SNe in the literature, providing a template library representing all suitable core-collapse SNe. We also provide the general software implemented to build this library, allowing an easy expansion for SNe published in the future.

The paper is laid out as follows. A detailed description of our techniques is presented in Section 2. In Section 3, we then select from the literature a sample of 67 well-observed core-collapse SN events for use in constructing our templates, and discuss various challenges in using the data to build the templates. We then illustrate the use of our new library by combining with published estimates of SN rates and LFs (Section 4.1), and simulating core-collapse SN contamination in a large photometric SN survey (Section 4.2.1). We present the results and the conclusions drawn from these tests in Section 5. Where relevant, we assume a Hubble constant of $H_0 = 70 \text{ km s}^{-1} \text{ Mpc}^{-1}$ and a flat, Λ CDM universe with a matter density of $\Omega_M = 0.3$.

2 METHOD

In this section, we present the techniques designed to construct time-series spectral templates from photometric and spectroscopic observations of individual SN events. Fig. 1 shows a schematic overview of the technique. (Our method assumes that any photometric data have been corrected for Milky Way and host galaxy extinction at the first order; we discuss this in detail in Appendix A and when applying the code to data in Section 3.)

We first interpolate the observer-frame SN light curves observed in multiple filters (Section 2.1), and we use this to estimate for each filter the photometric flux at the epochs on which spectral information for the SN is available. The interpolated photometry is then used to ‘flux-calibrate’ the observed spectra by adjusting the overall spectral shape, but retaining the detailed spectral features (Section 2.2). We then use UV photometry from the same SN event to extend the spectral templates at bluer wavelengths (Section 2.2.1). Finally, we smoothly interpolate between the (UV extended) calibrated spectra so that the final time series is sampled daily (Section 2.3). We discuss each step in turn.

2.1 Light-curve fits

We explored various techniques to fit or model the SN observer-frame light curves, using different parametric forms. This included testing different models proposed in the literature (Vacca & Leibundgut 1996; Bazin et al. 2009; Kessler et al. 2010b; Karpenka et al. 2013; Sanders et al. 2015), and exploring different techniques

¹https://c3.lbl.gov/nugent/nugent_templates.html

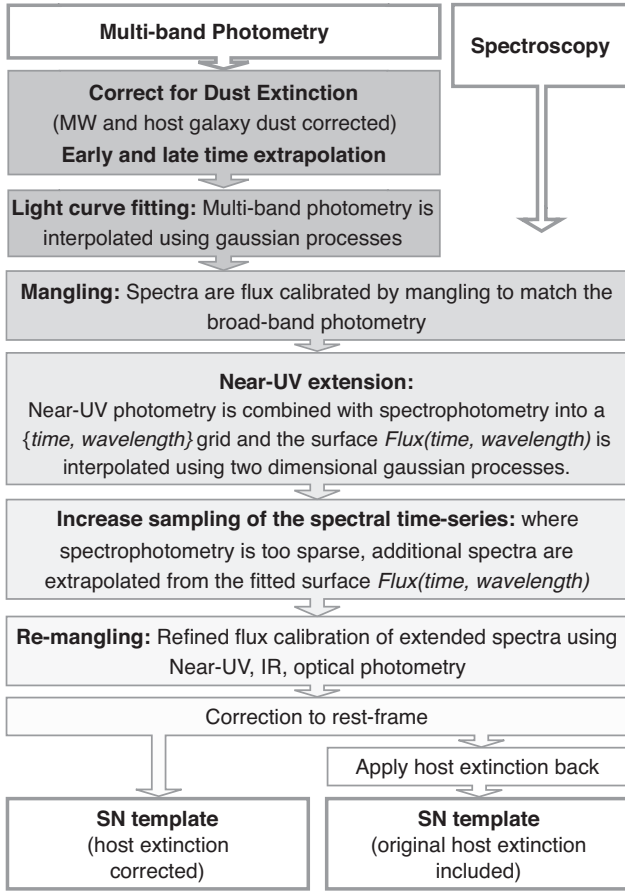


Figure 1. Schematic of the process used to build SN spectral templates from multiband photometry and spectroscopy. The final templates are sampled daily and extended into the near-UV. The technique implemented to fit multiband light curves is presented in Section 2.1, and the flux calibration and near-UV extension of the spectroscopic data are discussed in Section 2.2. In Section 2.3, we explain the final corrections applied to produce the final SN template.

to fit these parametric forms, including the MULTINEST package (Feroz & Hobson 2008; Feroz, Hobson & Bridges 2009) and the MPPFIT package (Markwardt 2009). However, we found no single functional form that had a sufficient flexibility to provide good fits across all filters for all core-collapse SNe, but yet that could still be reliably constrained by typical SN data. For this reason, we opted instead to use a non-parametric data-driven interpolation technique, Gaussian processes (GPs).

2.1.1 Modelling light curves with Gaussian processes

There are now several examples in the literature of the use of GPs (Rasmussen 2006) to interpolate transient light curves or SEDs (Kim et al. 2013; Angus et al. 2019; Inserra et al. 2018; Saunders et al. 2018). A GP can be seen as the generalization of a multivariate Gaussian distribution. Formally, a GP generates data located throughout some domain (time, in the case of light curves) such that any finite subset of points in that domain follows a multivariate Gaussian distribution. As a multivariate Gaussian distribution is fully specified by its mean and covariance matrix, a GP is defined by a mean function and the covariance function, $k(x, x')$ (also called the kernel), that relates each point (of the light curve in this case)

to any other. The hyperparameters needed to define the kernel are usually determined using a likelihood maximization routine.

Regression using GPs has several advantages. The first is that GP regression is a non-parametric model, and therefore has the flexibility to interpolate the wide heterogeneity of light-curve shapes inherent in core-collapse SNe. Secondly, it is straightforward to include in the model the uncertainties of the observed photometric data points and, consequently, to estimate uncertainties on the interpolated light curve. However, while the ‘function-agnostic’ nature of GP is a strength, the downside is that GPs are also physics-agnostic. As a consequence, negative fluxes, and diverging and infinitely brightening light curves are, in principle, allowed. However, these non-physical behaviours typically occur when light curves are extrapolated outside the time range covered by the photometric data, which can be avoided by restricting to interpolation only.

We use the python package GEORGE (Ambikasaran et al. 2015) to perform the GP regression on the light curves in flux space. We use a Matern 3/2 kernel function (k) of the form

$$k(x, x') = A \left(1 + \frac{\sqrt{3}(x - x')}{\sigma} \right) \exp \left(-\frac{\sqrt{3}(x - x')}{\sigma} \right), \quad (1)$$

where A is an amplitude factor, σ regulates the scale at which correlations are significant, and x is the domain over which the regression is being performed, which in this case is time. Generally, we optimize the free hyperparameters of the model (amplitude and scale of the kernel function) by minimizing the log likelihood of the model given the data, and we set the prior on the mean function to a constant zero function.

2.1.2 Early and late phases

The GP interpolation works well at most light-curve phases, but requires extra attention at the start and end of the light curve (where photometric sampling is sparser or absent) to ensure that the interpolation is robust.

At late phases, the SN luminosity is powered by ^{56}Co decay. Sparse photometric measurements are sufficient to constrain the SN evolution in this phase, so SNe are typically observed less frequently. However, when the data become sparser, the GP interpolation becomes less informative, and with larger uncertainties. We therefore visually inspect each light curve and determine at which phase it becomes dominated by ^{56}Co decay. We then interpolate/extrapolate additional photometric points and propagate their uncertainties from the linear fit for use in the GP interpolation. This ‘oversampling’ of the light curve significantly improves the GP interpolation, without adjusting the original data around peak.

At early phases, we use a similar approach and oversample the rising part of the light curve, filling the gap between the estimated explosion day and the first photometric data point. We fit the early data flux f as a function of time t with a widely used parametrization of

$$f(t) = \begin{cases} \alpha(t - t_0)^n, & \text{if } t \geq t_0, \\ 0, & \text{if } t < t_0, \end{cases} \quad (2)$$

where α is a normalization coefficient, t_0 is the time of explosion, and n is the power index of the rising light curve.

For most of the SNe, an accurate estimate of t_0 can be found in the literature, typically derived from light-curve modelling or from the analysis of early spectroscopic observations (e.g. Drout et al. 2016). Thus, we generally fix the parameter t_0 . When the explosion epoch is uncertain, we treat t_0 as a free global parameter and use non-detections and the SN date of discovery as lower and upper bounds

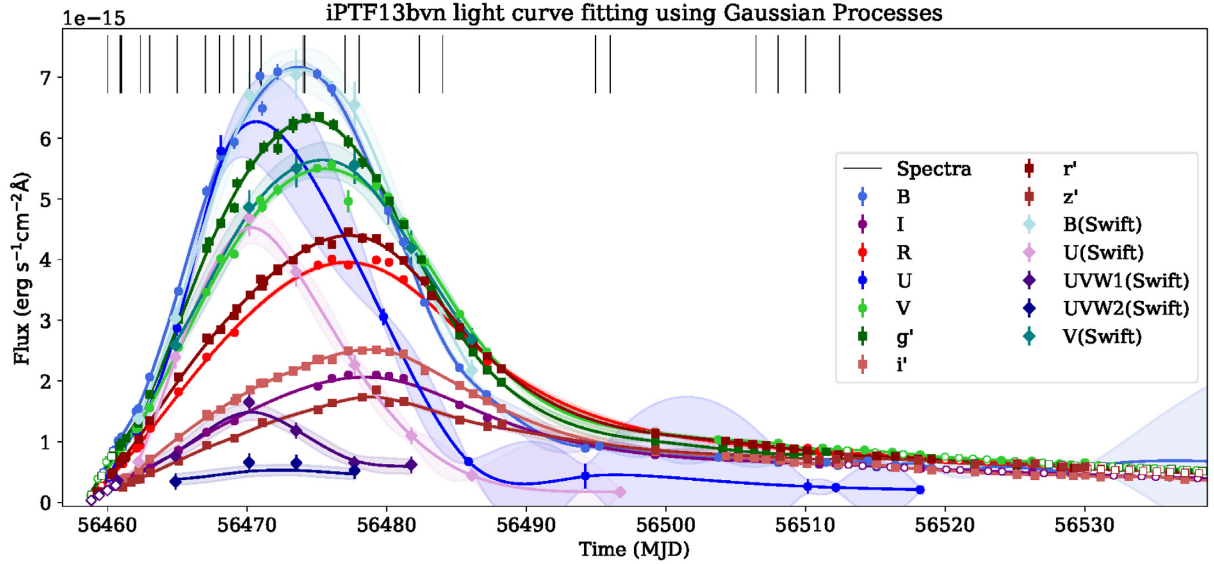


Figure 2. Fit of multiband light curves using GPs for the SN Ib iPTF13bvn. iPTF13bvn was observed in 14 filters, including 5 filters from *Swift*/UVOT. Filled dots indicate the published photometry. The cobalt decay dominated phase of each light curve is artificially oversampled to better constrain the GP interpolation at later phases, denoted with open symbols (see Section 3.2). Solid lines show the interpolation estimated using GPs, and the shaded area shows the uncertainty on this interpolation. The black vertical lines indicate epochs at which spectra were obtained.

on t_0 . The power index n is fixed only when the available early photometry is too poor to constrain the fit. For stripped-envelope SNe, we assume a power law of the form $f(t) \propto t^{1.5}$, expected for the cooling of the shock-heated expanding ejecta (Piro & Nakar 2013). For hydrogen-rich SNe, we assume $f(t) \propto t^{0.935}$ (González-Gaitán et al. 2015).

For some SNe considered (SN 1987A, SN 1993J, SN 2006aj, SN 2013df, SN 2011dh, and SN 2011fu), an initial shock breakout is detected in the light curves, presenting as an initial peak in the photometry. In such cases, the fitted functional form used is

$$f(t) = \begin{cases} \alpha(t - t_0)^n + \mathcal{N}(t_b, \sigma_b)(1 - e^{t-t_0}), & \text{if } t \geq t_0, \\ 0, & \text{if } t < t_0, \end{cases} \quad (3)$$

where t_b and σ_b are the peak and width of the initial bump in the light curve.

Fig. 2 shows an example of a multicolour light-curve interpolation using GPs for the SN iPTF13bvn (Fremming et al. 2014). Equivalent figures for all other events in our sample are available as online-only figures.

2.2 Generating spectrophotometric data

Observed SN spectra are rarely spectrophotometric, no matter how carefully the observations and reductions are performed. Differential slit losses during the observation, centring errors of the object on the slit, or non-photometric observing conditions not only affect the overall normalization of the spectrum, but can also introduce a smooth, wavelength-dependent distortion of the continuum (Buton et al. 2013).

Multiband photometry allows a correction to be made for many of these effects: it can set the overall flux normalization, and also provides information on the broad-band colours of the spectrum. We therefore adjust the observed spectra so that they match, in colour space, the photometry interpolated at the epoch of spectral observation. This correction is sometimes referred to as ‘mangling’ the spectrum (e.g. Hsiao et al. 2007; Conley et al. 2008), and consists

of determining a smooth wavelength-dependent function that, when multiplied by the original spectrum, produces a spectrum with the correct colours and normalization. In order to calculate this smooth wavelength-dependent function, we again use GPs.

For each SN spectrum, we first calculate the observed flux in each of the filters for which a photometric light curve is available. We compare these synthetic fluxes with the photometry interpolated from the light curve (Section 2.1), and determine the ratio of the two, propagating the uncertainties from the GP light-curve interpolation and from the spectrum. We place each calculated ratio at the filter effective wavelength of the original spectrum, and use GPs to interpolate as a function of wavelength, obtaining a smooth wavelength-dependent calibration function. We use again a Matern 3/2 kernel (equation 1), fixing the scale to 300 Å.

We do not use the common approach of using spline interpolation in the mangling. We explored this approach in detail, but found it is difficult to account correctly for the observational uncertainties in the photometry. The spline interpolation can also produce discontinuities in the mangling function for SNe for which photometry in neighbouring filters with close effective wavelengths is available (e.g. SNe that have photometry in both SDSS r and Bessell R). Fig. 3 shows an example of a mangled spectrum and the interpolated mangling function.

2.2.1 Extending the wavelength coverage of the spectra

During the mangling procedure described earlier, any near-UV or near-IR data from the SN are not used, as the spectroscopic data typically cover the optical wavelength range.² However, near-UV coverage in the SN rest frame is critical to simulate SN events at higher redshift (i.e. typically at $z > 0.2$). We therefore use near-UV

²Less than 10 per cent of the spectra considered in Section 3 have coverage below 4000 Å and only 50 per cent cover >9000 Å.

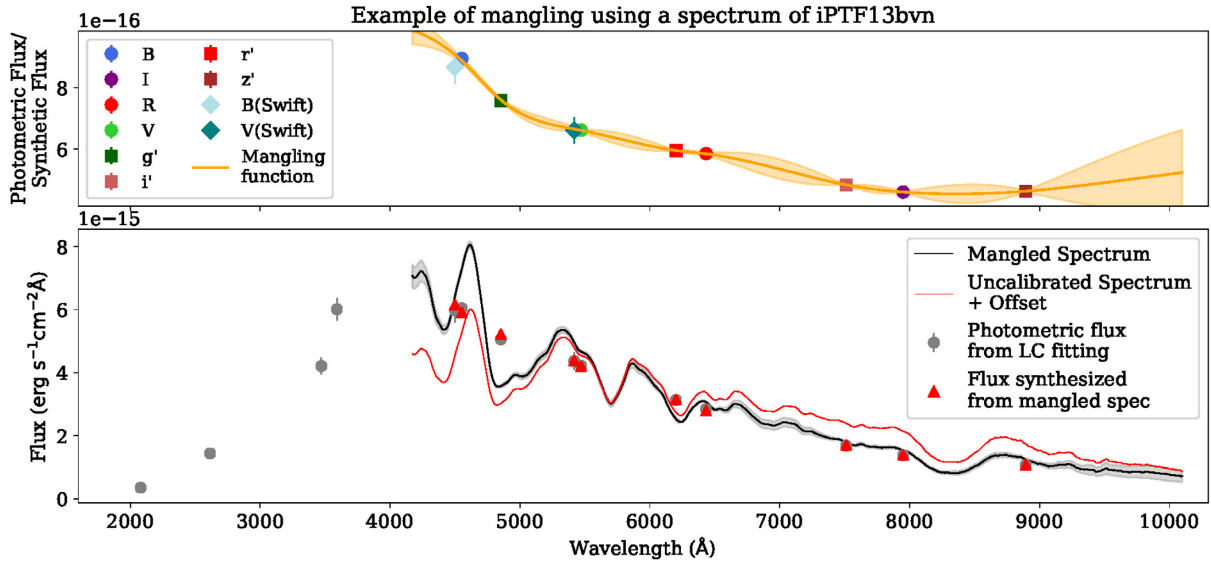


Figure 3. Mangling of the iPTF13bvn spectrum taken at MJD 56469.0. *Top panel:* For each filter, we show the ratio between the photometric flux (estimated using the GP interpolation of the light curve at the epoch of spectral observation) and the synthetic flux from the observed spectrum. The uncertainties from the light-curve GP interpolation are propagated. The smooth mangling correction function is also interpolated using GPs (solid orange line). *Lower panel:* The comparison between the observed spectrum (red line) and the ‘flux-calibrated’ spectrum following the mangling technique (black line). The photometric fluxes estimated from the light-curve interpolation are shown for each filter as grey dots. The fluxes synthesized from the flux-calibrated spectrum are also shown (red symbols) for comparison. Given the limited wavelength coverage of the spectrum in the near-UV, the photometry in the bluer filters is not used in the mangling process, but is used later to extend the spectrum into the near-UV.

photometry observed for the same SN to smoothly extrapolate the spectra to lower wavelengths.

We experimented with smoothly extrapolating the spectrophotometric data by fitting a blackbody function to the optical and near-UV photometry. While this works for the rather featureless very early spectra of some SN subtypes, it provides a poor near-UV representation for most of the SN events we consider. The complex absorption due to ionized metals present in the SN envelope typically dominates the UV part of the SN SED during most of its evolution, and its modelling is non-trivial (Gal-Yam et al. 2008; Bufano et al. 2009; Ben-Ami et al. 2012, 2015). We therefore decided to use a less rigid approach and again implement GPs. In this case, we combine photometry (i.e. integrated flux versus time, t) and spectrophotometry (i.e. flux density versus wavelength, λ) into a two-dimensional grid on which we can interpolate a flux surface $f(t, \lambda)$.

The implementation of a two-dimensional interpolation of this flux surface $f(t, \lambda)$ presents several advantages. First, it guarantees that the near-UV extension is continuous in time; extending each spectrum individually can result in large discontinuities in the final spectral time series in the near-UV. In addition, it is common to have spectroscopic observations of the same SN from different facilities. As a result, the wavelength coverage of the available spectra can change significantly from spectrum to spectrum, with some spectra extending to ~ 3200 Å, while other ending at 4000 – 4500 Å. A two-dimensional interpolation allows us to perform an extension including any information from adjacent spectra, and provides a final template that is continuous in time. Moreover, a two-dimensional model allows us not only to extend the spectrophotometry into the near-UV or near-IR, but also to simultaneously smoothly interpolate between the spectra and extrapolate *additional* spectra when the available data are too sparse (see Section 2.3).

In order to interpolate the flux surface $f(t, \lambda)$, both photometric and spectrophotometric data are combined and smoothed on a grid with a 60 Å binning in wavelength (to uniformly sample all the calibrated spectra and reduce the number of data points used to train the GP model). An example is shown in Fig. 4. The UV integrated flux is included and placed on the wavelength axis at the mean wavelength of the filter. The kernel used for GP interpolation is a two-dimensional Matern 3/2 kernel function (equation 1), where x is now the two-dimensional vector $\mathbf{x} = \{x_t, x_\lambda\}$. The GP hyperparameters σ_λ and σ_t are fixed to 100 Å and 30 d, respectively (optimizing these hyperparameters does not affect the results significantly and is computationally expensive).

The two-dimensional GP interpolation requires a prior for the mean function to prevent non-physical behaviour (i.e. negative fluxes or a GP model rapidly decreasing to zero when the data coverage is poor) from occurring. Building this prior is not trivial given the diversity of core-collapse SNe in terms of brightness, shape, and colours. In order to do this, we use observed data from the 67 core-collapse SNe that we will introduce in Section 3, examining their colour evolution in the optical and near-UV after dust extinction corrections (these SNe are all at $z < 0.03$ where k -corrections are small). To first order, SNe II and fast rising SNe IIn (hydrogen-rich SNe) present a similar colour evolution, despite having different absolute brightnesses. The same is true for the stripped-envelope SN classes of SNe Iib, SNe Ib, and SNe Ic/Ic-BL (see also Drout et al. 2011; Stritzinger et al. 2018b) and for the subclass of slow rising SNe IIn like SN 2006aa and SN 2011ht.

First, we measure, for each SN and for each optical and near-UV filter X , the evolution of $F_X(t)/F_V(t)$, where F_X and F_V are the GP interpolated light curves in filters X and the V band, respectively. We then average $F_X(t)/F_V(t)$ over all SNe within the same subclass

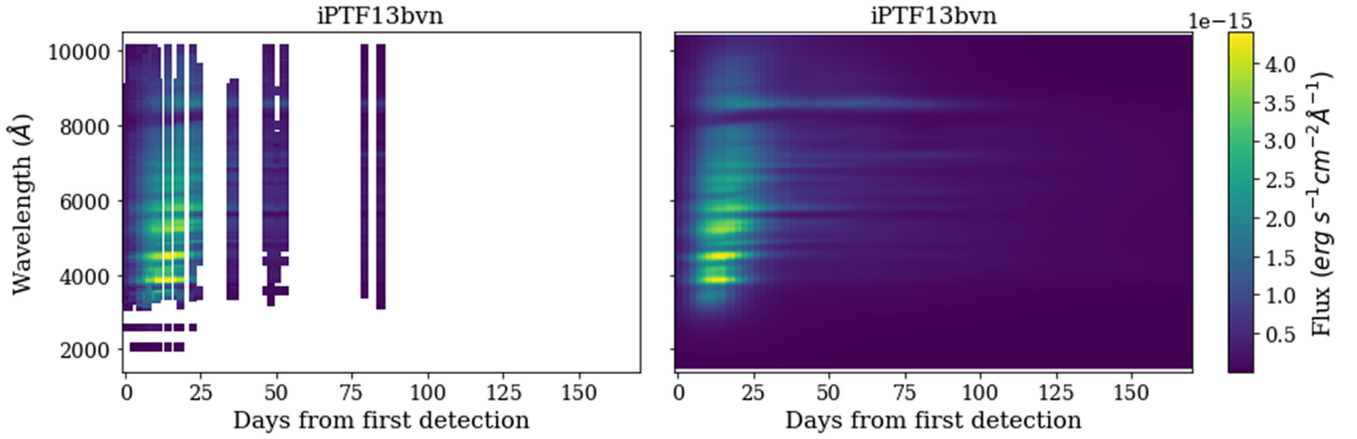


Figure 4. *Left:* Two-dimensional surface built for the SN Ib iPTF13bvn, combining sparse flux-calibrated spectroscopy and near-UV photometry as described in Section 2.2.1. For this SN, photometry in the *Swift* filters *u*, *uvw1*, and *uvw2* is available. In this graphical representation of the two-dimensional flux surface $f(t, \lambda)$, spectrophotometry is represented by continuous vertical stripes, and light-curve photometry by horizontal stripes. *Right:* The smoothed interpolation of the flux surface $f(t, \lambda)$ surface using two-dimensional GPs.

(hydrogen-rich, stripped-envelope, or slow SNe IIn). We also measure, in each filter, the average wavelength weighted by a typical hydrogen-rich, stripped-envelope, or slow Type IIn SED. We interpret each average colour evolution $\langle F_X(t)/F_V(t) \rangle$ as a monochromatic measurement of colour at the respective average wavelength, and we smoothly reconstruct the ‘colour surface’ $\langle F_{X-V}(t, \lambda) \rangle$. For each SN, the prior used to interpolate the flux surface $f(t, \lambda)$ is calculated multiplying the ‘colour surface’ $\langle F_{X-V}(t, \lambda) \rangle$ by the *V*-band light curve of the SN itself. This means that for each SN we build a different prior that has the colour properties of the subclass of SNe it belongs to, but is still normalized to the apparent brightness of the SN considered.

We test the effects of our prior using some of the best observed SNe (e.g. SN 2013by and iPTF13bvn). We perform the two-dimensional GP interpolation with and without the prior, using the full set of data available for the SN, and then removing some information (i.e. simulating reduced UV coverage or sparser spectroscopy). We find that the choice of the prior improves the results when sparser data or less UV coverage is available, without significantly overestimating or underestimating the final near-UV extension, and without affecting the accuracy of the spectrophotometry.

Once the prior is built, the flux surface $f(t, \lambda)$ is interpolated and it is then straightforward to extrapolate for each optical spectrum the near-UV extension. Fig. 5 shows an example of spectra observed for the SN Ib iPTF13bvn and extended applying the technique presented in this section. In Fig. 4, we show, for the same SN, a graphical representation of the flux surface $f(t, \lambda)$ as reconstructed from the two-dimensional GP.

2.2.2 Refining the calibration of the extended spectra

The extended spectra reconstructed from the two-dimensional interpolation provide a good approximation of the underlying near-UV SED. However, when building the two-dimensional surface, we interpret the photometric measurements as monochromatic flux density measurements at the filter mean wavelength. Ideally, the effective wavelength – λ_{eff} , the average wavelength of the filter weighted by the SED – should be used instead, but this is not known a priori as the SED is not known. This can lead to inaccuracies, particularly in the near-UV when using photometry from *Swift*

(Brown et al. 2016), where the filter transmission functions present significant tails into the optical. This can be relevant for some core-collapse SNe with strong UV variability or at very early phases. As a consequence, the (time-dependent) filter effective wavelength can be significantly different from the filter mean wavelength as the SED changes, and as a result, fluxes synthesized from our extended spectra in the *Swift* filters can be up to 40–50 per cent discrepant when compared to the observed photometric fluxes.

We address this by adjusting the near-UV fluxes to remove the optical contribution from the filter red leaks before including them in the two-dimensional grid for interpolation. We do this by integrating the spectra over each filter’s optical tail, subtracting from the original *Swift* photometry, and then using this subtracted photometry in the two-dimensional grid for the interpolation. After the spectral time series is extended, we then apply a further correction to the final extended spectra. For each extended spectrum, we compute synthetic photometry in the near-UV and optical filters, and compare with the original photometry observed in the same filters. We then adjust the extended spectra until the synthetic and observed photometry match. We apply this process iteratively as λ_{eff} for each filter changes as the spectrum is mangled. We refer to this additional correction as ‘remangling’. At the end of this process, the extended spectra are robustly flux-calibrated at all wavelengths.

During the remangling, the GP model provides not only a prediction of the mangling function, but also the relative full covariance matrix. This includes the uncertainties on the input photometry (added in quadrature to the diagonal of the covariance matrix of the GP model) and provides a robust estimate of the (highly correlated) uncertainties on the final flux-calibrated spectrum.

2.3 Final templates

The most widely used SN simulation packages usually simulate SN light curves by synthesizing broad-band photometry from a spectral time-series model, and then linearly interpolating between this synthetic photometry to generate a light curve at any required cadence. For this reason, the optimal time sampling for our final time-series SED templates is approximately 1 or 2 d, for a total phase coverage from a few days prior to maximum brightness to around a hundred days after maximum brightness. The observed photometry

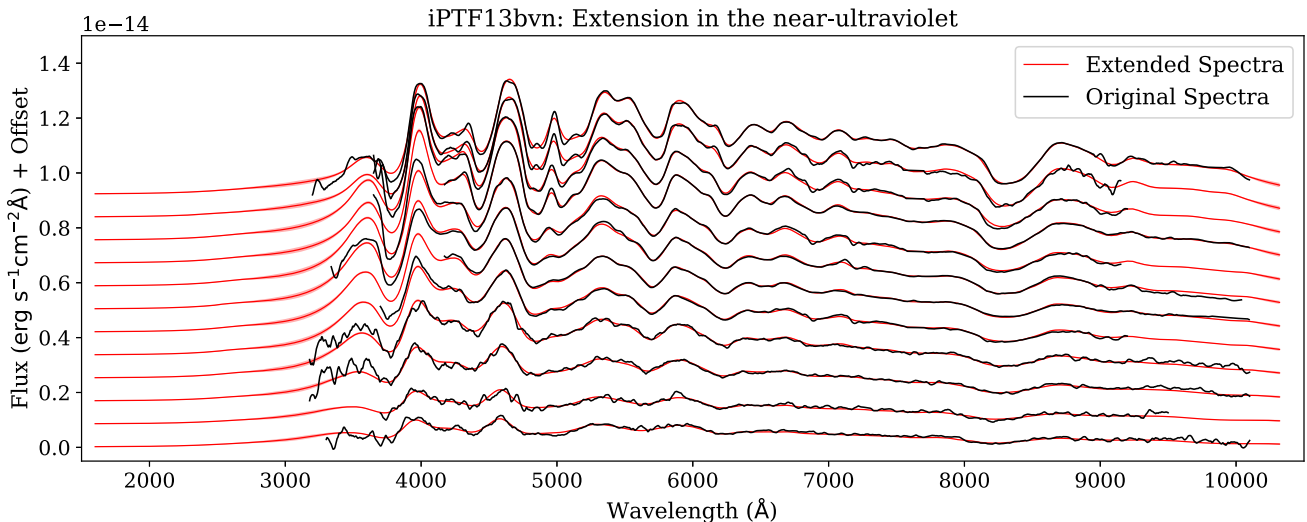


Figure 5. Near-UV extension of spectrophotometric observations for the SN Ib iPTF13bvn. Each flux-calibrated spectrum (black) is extended using near-UV light curves and the two-dimensional interpolation technique presented in Section 2.2.1. The near-UV extended spectra are shown in red.

for our SN events typically meets this quality of sampling. However, the spectroscopic observations generally have a significantly lower cadence and poorer phase coverage.

We therefore increase the time sampling of our templates by smoothly interpolating between the calibrated spectra. This smooth interpolation is performed as described in Section 2.2.1, and an example is shown in Fig. 4. Additional spectra are extrapolated from the interpolated flux surface and then remangled as described in Section 2.2.1, ensuring that the colours and normalization of the synthetic extrapolated spectra data are accurate.

As a final step, we transform each template to the rest frame using the measured heliocentric redshift. When necessary, corrections for peculiar velocities are applied. Each SN template is daily sampled and its phase is calibrated arbitrarily by defining day 0 as the day at which the synthesized *BVR*I pseudo-bolometric light curve reaches its maximum value.

The result is a daily sampled and de-reddened, rest-frame spectrophotometric template. These templates can be used for simulations of SN light curves up to $z \approx 1$, in any optical filter system and assuming any Milky Way or host galaxy dust reddening. We also provide templates for which host galaxy extinction has not been corrected. In Fig. 6, we present synthetic photometry simulated at different redshifts in the LSST filter system using the SN template built from the SN Ib iPTF13bvn.

These template SEDs can be easily integrated in SN simulation packages such as Supernova Analysis software (SNANA; Kessler et al. 2009) or SNCOSMO (Barbary et al. 2016). The Python package used to generate the templates is also available,³ along with examples and tutorials.

3 DATA

We now describe the data from which we can use the techniques described in the previous section to construct a series of core-collapse spectral templates. We do this using 67 core-collapse SNe for which high-quality photometry and spectroscopy has been

published. We describe the selection criteria we applied to build this data set, and various other data preparation procedures.

3.1 Description of the data set

3.1.1 Selection criteria

We select core-collapse SNe from the literature according to the following criteria:

- (i) The published SNe must have photometric data in at least the three optical filters of *B*, *V*, and *R* (or alternatively *g*, *r*, and *i*), with a well-constrained light-curve interpolation and at least one epoch prior to peak brightness in the *V* (or *g*) band.
- (ii) The SNe must have photometry in at least one near-UV filter, i.e. a filter that samples the wavelength range below 4000 Å in the SN rest frame. This near-UV photometry must have at least one epoch within 2 d of the *V/g*-band peak.
- (iii) The SNe must have at least five spectra, with at least one observation within 3 d of the *V/g*-band peak, and at least one observation after +15 d.

We do not apply any redshift constraints, and in principle our technique can be applied to SNe observed at any redshift. However, multiple spectroscopic follow-up observations of SNe become expensive at redshifts above $z \sim 0.05$, and thus mostly nearby SN events have been included in this work.

We found 67 core-collapse SN events in the literature that satisfy these quality cuts. This sample is presented in Table 2. Where available, we download the spectra from the WISerEP repository⁴ (Yaron & Gal-Yam 2012) and the photometry from the ‘Open Supernova Catalog’ (Guillochon et al. 2017).

3.1.2 UV data

Since all SNe selected are at low redshift ($z < 0.03$; Table 2), near-UV photometry in the SN rest frame corresponds to observations in the observer-frame *U* band or bluer filters. For 36 of the

³<https://github.com/maria-vincenzi/PyCoCo>

⁴<https://wiserep.weizmann.ac.il/>

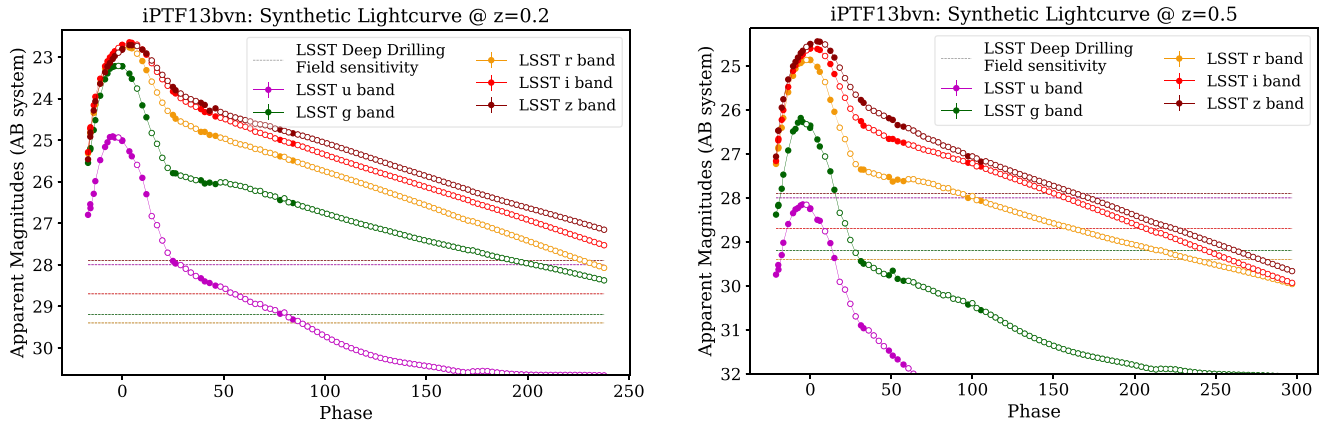


Figure 6. Synthetic multiband photometry estimated using the SN template built from the SN Ib iPTF13bvn. The photometry is synthesized in the LSST filter system, with the SN event simulated at $z = 0.2$ (left-hand panel) and $z = 0.5$ (right-hand panel). Filled symbols indicate photometric points synthesized from calibrated and extended spectroscopic observations; open symbols indicate photometric points synthesized from spectra extrapolated from the flux surface $f(\lambda)$ (see Section 2.3). For comparison, we show for each filter the sensitivity estimated for the LSST Deep Drilling Fields. Equivalent figures for all other events in our sample are available as online-only figures.

67 SNe selected in this work, UV photometry is measured by *Swift*/UVOT (Brown et al. 2014) using four UV filters (and two optical filters) for imaging, and two grisms for low-resolution spectroscopy. The central wavelengths for the near-UV filters are 3465, 2600, 2246, and 1928 Å for the filters *u*, *uvw1*, *uvw2*, *uvw2*, respectively.

3.1.3 Host galaxy extinction estimates

Providing a library of host galaxy extinction-corrected core-collapse SN templates is a significant advantage, especially when using these templates in simulations, as arbitrary amounts of extinction can then be added. Thus, the input to our template construction method in Section 2 should be extinction-corrected photometry.

However, estimating SN extinction due to local host galaxy dust is challenging as indicators of dust extinction are difficult to measure. We discuss various methods and resources used to estimate the SN host galaxy extinction in Appendix A. In Table 2, we report for each SN the values adopted for reddening due to dust in the SN host galaxy, $E(B - V)^{\text{host}}$. We note that our code will make the required corrections to the SN photometry provided the extinction estimates (i.e. $E(B - V)$) are given.

3.1.4 Supernova classification scheme

In the application of our library of templates for simulations, and for training supervised machine learning classifiers, we require a broad classification scheme. Given the limited number of objects available in our data set, we group our templates into six spectral subtypes: SN Ib (13 SNe), SN Ic (7 SNe), SN Ic-BL (6 SNe), SN IIb (11 SNe), SN II (23 SNe), SN IIn (7 SNe), and SN 1987A.

We do not apply the historical distinction between SNe IIP and SNe IIL, as recent analyses show reduced evidence for such a separation (Anderson et al. 2014). The sample of 23 SNe II considered in this work presents a continuum of decline rates, from small decline rates and almost flat light curves, to fast-declining events fading at around 1 mag per 30 d.

We also include in our sample more recently identified subclasses of peculiar SNe, such as SNe Ibn (SN 2010al), and other peculiar SN

IIn events (IIn-pec) such as SN 2009ip. SNe Ibn/IIn-pec represent very interesting classes of rare transients: their luminosities can be comparable to SNe Ia and their light curves are not necessarily as wide as normal SNe II. However, the lack of unbiased samples of these classes of transients, and their diversity, makes it difficult to measure their global properties (e.g. their luminosity distribution or relative rates); therefore, we combine SNe Ibn and SNe IIn-pec into a single group of SNe IIn. In Table 2, we report the list of SNe included in this work and the spectroscopic type.

3.2 Implementation

The data that we use to build the spectral templates are generally used as published. However, in the implementation phase it is sometimes necessary to remove observational and astrophysical signatures that do not have a SN origin, or that are not relevant for the purpose of these templates. We also apply some basic data conversions and noise reduction procedures as follows:

- (i) As the light-curve interpolation is always performed in flux space, we convert photometric measurements from magnitudes to flux densities. For the conversion of photometry to flux densities, we use our own custom-written software.⁵
- (ii) We correct the photometry for Milky Way and host galaxy extinction using a Cardelli, Clayton & Mathis (1989) dust law with $R_V = 3.1$. For Milky Way extinction, we use the Schlegel, Finkbeiner & Davis (1998) dust maps. We discuss in detail our choice of $R_V^{\text{host}} = 3.1$ in Appendix A.
- (iii) Some older events (e.g. SN 1987A, SN 1993J) do not have published uncertainties on their magnitude measurements. We arbitrarily estimate the uncertainties as 10 per cent of the fluxes.
- (iv) Photometric observations taken on the same night and in the same filter are averaged in order to reduce uncertainties in the individual measurements.
- (v) Using a sigma-clipping algorithm, we remove spectral features clearly associated with a host galaxy (e.g. nebular emission lines) or due to the atmosphere (telluric features).

⁵https://github.com/chrisfrohmaier/what_the_flux

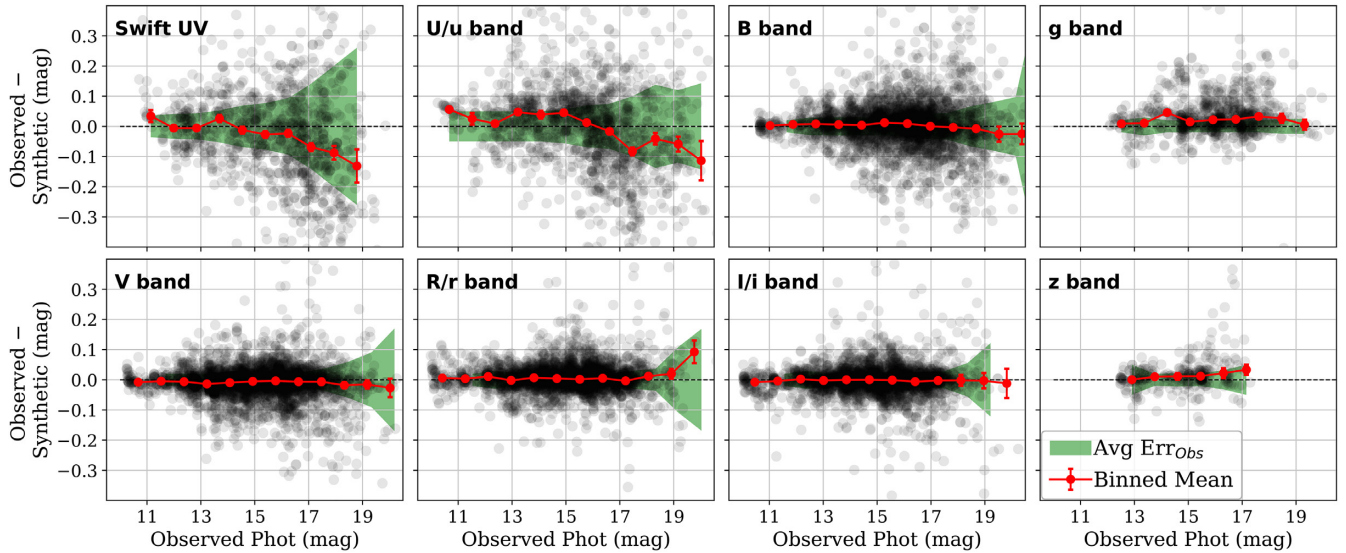


Figure 7. Observed photometry compared to photometry synthesized from the final templates of the 67 SNe in our sample. The observed photometry is the published photometry corrected for Milky Way and host dust extinction, and it is the same used to perform the light-curve fitting described in Section 2.1. Synthetic photometry at the same epoch of the observed photometry is measured from the final flux-calibrated, daily sampled, and near-UV extended spectral time series. For every SN, for every photometric point observed for the SN, the difference between observed and synthetic photometry is shown (black symbols) as well as the binned mean and error on the mean of the residuals. Each panel shows the residuals for different group of filters: UV filters (*Swift* filters *uvw2*, *uvm2*, and *uvw1*), *u* band (Bessell *U*, *Swift* *U*, SDSS *u* bands), *B* band (Bessell *B* and *Swift* *B* bands), *V* band (Bessell *V* and *Swift* *V* band), *g* band, *R/r* band (Bessell *R* and SDSS *r* bands), *I/i* band (Bessell *I* and SDSS *i* bands), and *z* band. Overall, we recover the observed photometry to within 0.02 mag in the optical bands and approximately 0.1 mag in the near-UV.

(vi) We smooth each spectrum by applying a Savitzky–Golay filter (Savitzky & Golay 1964) using a window of 100 Å.

Once the data have been pre-processed as described, we apply on them the technique presented in Section 2. In around 6 per cent of the light curves considered in our data set, the signal-to-noise ratio of the photometry is sufficiently low such that the GPs oversmooth the data. In such cases, we manually fix the scale of the kernel or use a non-zero prior on the mean function when performing the light-curve fitting described in Section 2.1.

After testing our technique on the sample of 67 SNe described in Section 3.1, we compare the published observed photometry with the photometry synthesized from the final flux-calibrated, daily sampled, and near-UV extended spectral time series. Our results are presented in Fig. 7. On average, the observed photometry is recovered to within 0.02 mag in most of the optical filters and to within 0.1 mag in the near-UV.

4 APPLICATION TO SIMULATIONS OF SN SURVEYS

Our new library of core-collapse SN templates has many potential uses in photometric SN classification and the simulations of optical transient surveys. In this section, we demonstrate their application to SN simulations by integrating our library of core-collapse SN templates into the SN light-curve simulation package SNANA. This requires two further key ingredients in simulating SNe, no matter what the scientific goal: the LF used to set the overall brightness distribution of the simulated events and the relative rates that different SN subtypes are simulated with. We then present an example application: the simulation of contamination by core-collapse SNe in cosmological surveys of SNe Ia.

4.1 Luminosity functions and relative rates

The LF describes the intrinsic distribution of brightnesses (absolute magnitudes) of SNe. Due to selection biases inherent in all astronomical surveys (or compilations/catalogues), it is difficult to measure accurately, with two main core-collapse SN LFs published in the last decade: Li et al. (2011, hereafter L11) and Richardson et al. (2014, hereafter R14).

The brightness distributions presented in L11 are measured from a volume-limited sample of 92 core-collapse SNe from the Lick Observatory Supernova Search (LOSS; Leaman et al. 2011). They are constructed in the *R*-band filter, and calibrated to the Landolt (1992) system from mostly unfiltered images with a precision of about 5 percent (Li et al. 2003). No *k*-corrections were made as the SNe all lie within 60 Mpc and thus *k*-corrections are small. In order to correct for potential biases in the volume-limited sample, L11 estimated for each SN the completeness of the LOSS survey within the fixed cut-off distance, given the brightness of the event. The peak absolute magnitude and light-curve shape of each SN are recovered by performing template fitting of the *R*-band light curve and then used in the computation of the completeness (see also Leaman et al. 2011). Different templates are used for SNe of different types. Each SN in the LF sample is then weighted by the reciprocal of this completeness.

Recently, Shivvers et al. (2017) revised the classifications of the SNe in the LOSS sample, and presented an updated measurement of the relative rate of each SN subtype. In particular, SNe IIL and IIP are now grouped into a single population (mirroring our templates), and calcium-rich SNe (Perets et al. 2010) and SNe Ic-BL are considered distinct classes. The classification of 15 SNe has also been corrected using additional spectroscopic observations. We use this reclassified LOSS sample to remeasure the LF of

Table 1. Summary of LFs and relative rates for core-collapse SNe.

SN type	LFs from L11 ^a	Revised LFs from L11 ^b	LFs from R14 ^c	LFs adjusted from Jones et al. (2017)	Rates ^d
II	–	– 15.97 (1.31)	–	–	64.9
IIIL	– 17.44 (0.64)	–	– 17.98 (0.86) ^e	– 18.28 (0.45)	7.9
IIP	– 15.66 (1.23)	–	– 16.75 (0.98) ^e	– 16.67 (1.08)	57.0
IIB	– 16.65 (1.30)	– 16.69 (1.38)	– 16.99 (0.92)	– 16.69 (1.99)	10.9
IIIn	– 16.86 (1.61)	– 17.90 (0.95)	– 18.53 (1.36)	– 17.66 (1.08)	4.7
Ic	– 16.04 (1.28)	– 16.75 (0.97)	–	– 17.44 (0.66)	7.5
Ib	– 17.01 (0.41)	– 16.07 (1.34)	– 17.45 (1.12)	– 18.26 (0.15)	10.8
Ibc-pec	– 15.50 (1.21)	–	–	–	–
Ic/Ic-pec/Ic-BL	–	– 16.79 (0.95)	– 17.66 (1.18)	–	8.6
Ic-BL	–	–	–	–	1.1

^aMean and rms. of the *R*-band absolute magnitudes in the bias-corrected sample from Leaman et al. (2011). No host extinction correction.

^bMean and rms. of the *R*-band absolute magnitudes in the bias-corrected sample, using the Shivvers et al. (2017) classifications. No host extinction correction.

^cMean and rms. of the *B*-band absolute magnitudes in the bias-corrected sample from R14. Host extinction corrections are applied.

^dRelative SN rates from Shivvers et al. (2017), with SN IIL and SN IIP rates taken from L11. Numbers are normalized to sum to 1.

^eR14 considered IIL and IIP as separate classes. We adapt our library of templates to this classification scheme when simulating core-collapse SNe using R14 LFs, and we define SNe IIL/IIP as SNe with decline rates above/below 1.1 mag per 100 d.

each core-collapse SN subtype, with SNe Ic, Ic-pec, and Ic-BL grouped into the same subclass due to the small numbers of events included in these classes (the relative fraction can be preserved in any simulations). We also exclude two SN IIIn now reclassified as SN imposters.

In principle, for each reclassified SN a new template fit and the recomputation of the completeness following L11 would be required. However, L11 used the same template for SNe Ib and SNe Ic, and thus SNe Ic reclassified as SNe Ib do not require new completeness calculations.

Other SNe that do require a new light-curve fit and for which the completeness should be recalculated are partially or completely excluded. This is the case of five SNe. SN 2003bw, SN 2003br, and SN 2005mg are reclassified from SNe II to SNe II/Ib. We can include them in SNe II LF but not in SNe IIB LF. SN 2004C and SN 2005lr are reclassified from SNe Ic to SNe IIB; therefore, we cannot include them in the SN IIB LF. These approximations are likely to bias the LF for SNe IIB. However, an accurate estimate of LFs goes beyond the purpose of this work. A comparison between the original L11 LFs and revised ones is shown in Table 1.

We also consider the LFs of R14. R14 measured LFs from a larger sample of 211 core-collapse SNe, combining the Asiago SN Catalog (Richardson et al. 2002, 2014) and supplementary magnitude-limited SN samples. These LFs are presented in the *B* band, and have additionally been corrected for host galaxy extinction. However, only half of the SNe considered (113 of 211) have specific information about host galaxy extinction, with an average *B*-band extinction of 0.292 mag assumed for the other events. Intrinsic biases in the SN sample are corrected using a bootstrap technique, and LFs measured from both the bias-corrected SN sample and a volume-limited but *not* bias-corrected SN sample. We test in our simulations the bias-corrected LFs (also reported in Table 1).

To determine the relative fraction of each core-collapse subtype, we use the revised nearby SN relative rates presented in Shivvers et al. (2017) (see also Table 1). These relative rates are assumed across all our simulations.

The LFs and the relative rates used in this section are all based on local SN measurements. In our simulations, we assume these LFs and relative rates also apply at higher redshift, i.e. we neglect any redshift evolution in these quantities. The only redshift dependence we assume is that of the global volumetric rate of all core-collapse SNe.

4.2 Simulating supernovae in cosmological surveys

SNe Ia can be used as standardizable candles to estimate distances in the universe (Riess et al. 1998; Perlmutter et al. 1999). Historically, samples of SNe Ia have been constructed where every SN Ia event has been spectroscopically confirmed and has a spectroscopic redshift measurement (e.g. Betoule et al. 2014; Scolnic et al. 2018). However, contemporary and future surveys will be unable to spectroscopically confirm every SN Ia event detected due to a lack of follow-up resources, and will therefore be reliant on photometric classification techniques based on a multicolour light curve and possibly a spectroscopic redshift of the SN host galaxy.

Contamination from events that are not SNe Ia is therefore potentially a serious problem (Campbell et al. 2013; Jones et al. 2017). Simulations can be used to estimate selection effects and the level of this contamination (Kessler & Scolnic 2017); a recent example can be found in Jones et al. (2017, hereafter J17) and Jones et al. (2018) using the PS1 photometric SN sample.

These simulations have analysed the ‘Hubble residual’ distribution for the SNe Ia in the sample. The Hubble residual is defined as $\mu_{\text{obs}} - \mu_{\text{model}}$, where μ_{obs} is the observed distance modulus for each SN event and μ_{model} is the theoretical distance modulus expected for the redshift of each event given a set of cosmological parameters. μ_{obs} is defined as

$$\mu_{\text{obs}} = m_B + \alpha x_1 - \beta C - M_B, \quad (4)$$

where m_B is the rest-frame *B*-band apparent magnitude at maximum light (or more accurately the log of the light-curve amplitude in the light-curve fit), x_1 is the SN ‘stretch’ parameter, C is the SN colour estimator, and α , β , and M_B are parameters defining the

Table 2. The core-collapse SNe included in this work.

Name	Type	Redshift	Peak M_B	Optical data	Near-UV data	Number of spectra	References ^a	$E(B - V)_{\text{host}}^b$	Reference host ^d
SN2013by	II	0.003 59	−18.36	<i>BVugri</i>	<i>u, v, uvw1, uvm2, uvw2</i>	7	(68), (69), (42)	0	(69)
ASASSN15oz	II	0.006 93	−18.19	<i>UBVRIgri</i>	<i>u, b, v, uvw1, uvm2, uvw2</i>	13	(2)	0	(2)
SN2014G	II	0.005 63	−18.10	<i>UBVRI</i>	<i>v, uvw1, uvm2, uvw2</i>	17	(77), (71), (78)	0.24	(78)
SN2007od	II	0.005 86	−17.93	<i>UBVRIri</i>	<i>u, b, v, uvw1, uvm2, uvw2</i>	13	(29)	0	(29)
SN2013ej	II	0.002 19	−17.76	<i>UBVRIgriz</i>	<i>u, b, v, uvw1, uvm2, uvw2</i>	28	(73)	0.049	(94)
SN2013fs	II	0.011 85	−17.73	<i>BVRIr</i>	<i>u, uvw1, uvm2, uvw2</i>	23	(74), (63), (42), (75)	0.015	(75)
SN2008bj	II	0.019	−17.48	<i>UBVri</i>		16	(31)	0.081 ^c	(90)
SN2016X	II	0.004 41	−17.38	<i>UBVRIgri</i>	<i>u, b, v, uvw1, uvm2, uvw2</i>	33	(79)	0.02	(79)
SN2009bw	II	0.003 82	−17.14	<i>UBVRI</i>	<i>uvm2, uvw2</i>	16	(39)	0.08	(39)
SN2013ab	II	0.005 32	−17.14	<i>BVRIgri</i>	<i>u, b, uvw1, uvm2, uvw2</i>	22	(64), (65)	0.02	(65)
SN2004et	II	0.001 05	−17.09	<i>UBVRI</i>		28	(16)	0.07	(87)
SN2012aw	II	0.0026	−17.05	<i>UBVRIugriz</i>	<i>u, b, v, uvw1, uvm2, uvw2</i>	30	(61), (62), (63)	0.028	(62)
SN2008in	II	0.005 22	−16.96	<i>BVri</i>	<i>u, b, v, uvw1, uvm2, uvw2</i>	10	(36), (31)	0.076	(36)
SN2009dd	II	0.002 46	−16.81	<i>UBVRIri</i>		6	(30), (31)	0.433	(30)
SN1999em	II	0.002 39	−16.69	<i>UBVRI</i>		27	(12)	0.077	(86)
SN2009kr	II	0.0065	−16.57	<i>BVRI</i>	<i>u, b, v, uvw1, uvm2, uvw2</i>	6	(44)	0	(44)
ASASSN14jb	II	0.006 03	−16.11	<i>BVgri</i>	<i>u, b, uvw1, uvm2, uvw2</i>	10	(1)	0	(1)
SN2012A	II	0.002 31	−16.10	<i>UBVRI</i>		39	(57)	0.012	(57)
SN2009ib	II	0.004 35	−15.86	<i>BVRIugriz</i>		9	(40)	0.131	(40)
SN2013am	II	0.002 69	−15.80	<i>UBVRIi</i>	<i>u, b, uvw1, uvm2, uvw2</i>	14	(66), (67)	0.55	(67)
SN2009N	II	0.003 45	−15.03	<i>BVRgriz</i>	<i>u, b, v, uvw1, uvm2, uvw2</i>	22	(37)	0.113	(37)
SN2005cs	II	0.001 54	−14.90	<i>UBVRIz</i>	<i>b, uvw1, uvm2, uvw2</i>	18	(23)	0.015	(89)
SN2016bkv	II	0.002	−14.89	<i>UBVRIgri</i>		15	(80), (81)	0	(81)
SN1987A	87A-like	0.000 01	−14.33	<i>UBVRI</i>		18	(3)	0.17	(85)
SN2011fu	IIf	0.0185	−18.62	<i>UBVRIz</i>		28	(52), (53), (21)	0.015	(53)
SN2006T	IIf	0.0081	−17.72	<i>BVugri</i>		6	(8), (19), (18)	0.277 (0.048) ^d	(88)
SN2008ax	IIf	0.0019	−16.65	<i>UBVRIugriz</i>	<i>u, b, v, uvw1, uvw2</i>	42	(34), (8), (24)	0.28	(91)
SN2016gkg	IIf	0.004 92	−16.61	<i>BVRIgr</i>	<i>u, b, v, uvw1, uvm2, uvw2</i>	17	(82)	0.09	(95)
SN2008aq	IIf	0.007 97	−16.60	<i>BVugri</i>	<i>u, b, v, uvw1, uvw2</i>	7	(8), (18)	0 (0) ^d	(88)
SN2011ei	IIf	0.0093	−16.60	<i>BVRI</i>	<i>u, b, v, uvw1, uvw2</i>	13	(50), (51)	0.18	(51)
SN2011dh	IIf	0.0015	−15.99	<i>UBVRIg</i>		39	(48), (49)	0.05	(49)
SN2013df	IIf	0.002 39	−15.90	<i>UBVRI</i>	<i>u, b, v, uvw1, uvm2, uvw2</i>	12	(70), (71), (72), (21)	0.08	(72)
SN2011hs	IIf	0.005 71	−15.71	<i>BVRIugriz</i>	<i>u, b, v, uvw1, uvw2</i>	13	(54)	0.16	(54)
SN2008bo	IIf	0.005	−15.46	<i>BVri</i>	<i>u, uvw1, uvw2</i>	13	(8), (24), (21)	0.033	(90)
SN1993J	IIf	−0.00 01	−13.22	<i>UBVRI</i>		50	(4), (5)	0.1	(5)
SN2008fq	IIn	0.0106	−18.89	<i>BVugri</i>		10	(35), (25)	0.46	(25)
SN2010al	IIn	0.017	−18.75	<i>BVRIluri</i>	<i>u, b, v, uvw1, uvm2, uvw2</i>	11	(45), (46), (31), (21)	0.053	(46)
SN2007pk	IIn	0.016 65	−18.71	<i>BVri</i>	<i>u, b, v, uvw1, uvm2, uvw2</i>	9	(30), (31)	0.081 ^c	(91)
SN2009ip	IIn	0.005 94	−18.33	<i>BVRI</i>	<i>u, uvw1, uvm2, uvw2</i>	55	(41), (42)	0.01	(91)
SN2006aa	IIn	0.0207	−17.61	<i>BVugri</i>		6	(25)	0.081 ^c	(90)
SN2011ht	IIn	0.0036	−16.98	<i>BVRI</i>	<i>u, b, v, uvw1, uvm2, uvw2</i>	12	(55), (56)	0.061	(56)
SN2005bf	Ib	0.0189	−18.44	<i>BVugri</i>		26	(22), (8), (18), (21)	0.1	(22)
SN2007uy	Ib	0.007	−18.34	<i>BVri</i>	<i>u, b, v, uvw1, uvm2, uvw2</i>	11	(8), (24), (21)	0.63	(93)
SN2005hg	Ib	0.021	−18.02	<i>UBVri</i>		20	(8), (24), (21)	0.2235 ^c	(90)
SN2009iz	Ib	0.0142	−17.69	<i>BVuri</i>	<i>uvw1</i>	10	(8), (24), (21)	0.2235 ^c	(90)
SN2009jf	Ib	0.008	−17.68	<i>UBVRIuugriiz</i>		31	(43), (8), (24), (21)	0.03	(91)
SN2004gv	Ib	0.02	−17.39	<i>BVugri</i>		5	(8), (18), (21)	0.053 (0.118) ^d	(88)
SN2012au	Ib	0.0045	−17.39	<i>BVRIz</i>	<i>u, b, v, uvw1, uvm2, uvw2</i>	5	(59), (60), (21)	0	(60)
SN2006ep	Ib	0.015	−17.16	<i>BVugri</i>		7	(8), (18), (21)	0.233 (0.226) ^d	(88)
SN2004gq	Ib	0.006 47	−16.97	<i>BVugri</i>		24	(8), (19), (18)	0.067 (0.143) ^d	(88)
SN1999dn	Ib	0.0093	−16.62	<i>UBVRI</i>		13	(11)	0.048	(11)
iPTF13bvn	Ib	0.004 49	−16.54	<i>UBVRIgriz</i>	<i>u, b, v, uvw1, uvw2</i>	25	(83), (84)	0.17	(84)
SN2008D	Ib	0.007	−16.47	<i>BVri</i>	<i>u, v, uvw1</i>	20	(33), (8), (24), (21)	0.6	(91)
SN2007Y	Ib	0.0046	−16.32	<i>BVugri</i>	<i>u, b, v, uvw1, uvm2, uvw2</i>	6	(27), (18), (21)	0.090 (0.318) ^d	(27)

Table 2 – continued

Name	Type	Redshift	Peak M_B	Optical data	Near-UV data	Number of spectra	References ^a	$E(B - V)_{\text{host}}^b$	Reference host ^a
SN2004aw	Ic	0.0159	−17.66	<i>UBVRI</i>		23	(15)	0.35	(15)
SN1994I	Ic	0.0015	−17.05	<i>UBVRI</i>		27	(6), (7), (8)	0.42	(7)
SN2004fe	Ic	0.018	−17.05	<i>BVugri</i>		9	(17), (8), (18)	0.000 (0.052) ^d	(88)
SN2004gt	Ic	0.005 48	−16.66	<i>BVugri</i>		13	(20), (8), (18), (21)	0.237	(88)
SN2013ge	Ic	0.0055	−16.57	<i>VRiri</i>	<i>u, b, v, uvw1, uvm2, uvw2</i>	18	(76)	0.047	(76)
SN2007gr	Ic	0.0017	−16.20	<i>UBVRIri</i>		36	(28), (8), (24), (21)	0.03	(92)
SN2011bm	Ic	0.0022	−13.10	<i>UBVRIugriz</i>		13	(47)	0.032	(47)
SN2006aj	Ic-BL	0.0334	−19.33	<i>UBVri</i>	<i>u, b, v, uvw1, uvm2, uvw2</i>	22	(26), (8), (24)	0.2	(91)
SN1998bw	Ic-BL	0.0085	−18.93	<i>UBVRI</i>		21	(9), (10)	0	(10)
SN2009bb	Ic-BL	0.01	−18.72	<i>BVugri</i>		12	(38), (18)	0.540 (0.200) ^d	(88)
SN2007ru	Ic-BL	0.0155	−18.65	<i>UBVRI</i>		5	(32), (8), (21)	0	(32)
SN2012ap	Ic-BL	0.0121	−17.66	<i>BVRI</i>	<i>u, b, v, uvw1</i>	12	(58), (21)	0.4	(58)
SN2002ap	Ic-BL	0.0022	−17.07	<i>UBVRI</i>		23	(13), (14), (8)	0.008	(14)

^aReferences: (1) Meza et al. (2019); (2) Azalee Bostroem et al. (2019); (3) Catchpole et al. (1987, 1988, 1989), Whitelock et al. (1988), and Pun et al. (1995); (4) Barbon et al. (1995) and Matheson et al. (2000a, 2000b); (5) Richmond et al. (1994); (6) Filippenko et al. (1995) and Clocchiatti et al. (1996); (7) Richmond et al. (1996); (8) Modjaz et al. (2014); (9) Galama et al. (1998); (10) Patat et al. (2001); (11) Benetti et al. (2011); (12) Hamuy et al. (2001), Leonard et al. (2002), and Galbany et al. (2016); (13) Gal-Yam, Ofek & Shemmer (2002), Foley et al. (2003), and Chornock et al. (2013); (14) Pandey et al. (2003); (15) Taubenberger et al. (2006); (16) Sahu et al. (2006), Maguire et al. (2010), and Faran et al. (2014a); (17) Harutyunyan et al. (2008); (18) Stritzinger et al. (2018a); (19) Shivvers et al. (2017); (20) Modjaz et al. (2008) and Taubenberger et al. (2009); (21) Shivvers et al. (2019); (22) Folatelli et al. (2006); (23) Pastorello et al. (2006, 2009) and Bufano et al. (2009); (24) Bianco et al. (2014); (25) Taddia et al. (2013); (26) Modjaz et al. (2006), Pian et al. (2006), and Sonbas et al. (2008); (27) Stritzinger et al. (2009); (28) Valenti et al. (2008) and Chen et al. (2014); (29) Inserra et al. (2011); (30) Inserra et al. (2013); (31) Hicken et al. (2017); (32) Sahu et al. (2009); (33) Mazzali et al. (2008) and Modjaz et al. (2009); (34) Pastorello et al. (2008) and Taubenberger et al. (2011); (35) Faran et al. (2014b); (36) Roy et al. (2011); (37) Takáts et al. (2014); (38) Pignata et al. (2009) and Pignata et al. (2011); (39) Inserra et al. (2012); (40) Takáts et al. (2015); (41) Mauerhan et al. (2013a), Fraser et al. (2013), Margutti et al. (2014), Graham et al. (2014), and Smartt et al. (2015); (42) Childress et al. (2016); (43) Valenti et al. (2011); (44) Elias-Rosa et al. (2010); (45) Shivvers et al. (2016); (46) Pastorello et al. (2015); (47) Valenti et al. (2012); (48) Arcavi et al. (2011), Tsvetkov et al. (2012), and Ergon et al. (2014); (49) Sahu, Anupama & Chakradhari (2013); (50) Milisavljevic et al. (2011); (51) Milisavljevic et al. (2013a); (52) Morales-Garoffolo et al. (2015); (53) Kumar et al. (2013); (54) Bufano et al. (2014); (55) Roming et al. (2012) and Humphreys et al. (2012); (56) Mauerhan et al. (2013b); (57) Tomasella et al. (2013); (58) Milisavljevic et al. (2015); (59) Milisavljevic et al. (2013b); (60) Takaki et al. (2013); (61) Bayless et al. (2013), Bose et al. (2013), and Munari et al. (2013); (62) Dall’Ora et al. (2014); (63) Rubin et al. (2016); (64) Silverman et al. (2017); (65) Bose et al. (2015a); (66) Khazov et al. (2016); (67) Zhang et al. (2014); (68) Black et al. (2017); (69) Valenti et al. (2015); (70) Silverman et al. (2012) and Van Dyk et al. (2014); (71) Yaron & Gal-Yam (2012); (72) Morales-Garoffolo et al. (2014); (73) Valenti et al. (2014), Bose et al. (2015b), Dhungana et al. (2016), and Yuan et al. (2016); (74) Valenti et al. (2016) and Bullivant et al. (2018); (75) Yaron et al. (2017); (76) Drout et al. (2016); (77) Bose et al. (2016); (78) Terreran et al. (2016); (79) Huang et al. (2018); (80) Nakaoka et al. (2018); (81) Hosseinzadeh et al. (2018); (82) Tartaglia et al. (2017); (83) Cao et al. (2013), Fremling et al. (2014), and Srivastav, Anupama & Sahu (2014); (84) Fremling et al. (2016); (85) Walker & Suntzeff (1990); (86) Krisciunas et al. (2009); (87) Zwitter, Munari & Moretti (2004); (88) Stritzinger et al. (2018b); (89) Baron, Branch & Hauschildt (2007); (90) Prentice et al. (2016); (91) Pritchard et al. (2014); (92) Hunter et al. (2009); (93) Roy et al. (2013); (94) Richmond (2014); (95) Arcavi et al. (2017b).

^bSource of the estimate is given in the Reference column. Unless otherwise indicated, reddening estimates presented in the table are derived from measurements of the equivalent width (EW) of the Na I D absorption lines, and applying an empirical relation $E(B - V)_{\text{host}} = 0.16 \text{ EW}_{\text{Na I D}}$ (Turatto, Benetti & Cappellaro 2003).

^cEstimate of host reddening not available. For this object, the median extinction estimated in Prentice et al. (2016) is used instead.

^dReddening inferred from colour evolution using the method presented in Stritzinger et al. (2018b). Estimates using the Na I D absorption lines are shown in parenthesis for comparison.

stretch–luminosity and colour–luminosity relationships for the SN Ia population being studied (e.g. Tripp 1998; Astier et al. 2006). The x_1 and C estimators are typically determined using the SALT2 light-curve fitter (Guy et al. 2007).

The set of simulations implemented for the cosmological analysis of the PS1 sample is presented in detail in J17. The parent distributions of x_1 and C used to simulate SNe Ia are determined by applying the method of Scolnic & Kessler (2016) to the PS1 spectroscopic SN sample (Rest et al. 2014) with additional adjustments, taking into account additional selection biases on the photometric sample. Core-collapse SNe are simulated using the set of 41 templates from the SNPhotCC library, with the addition of 4 new templates of SNe IIb built using more recent observations (models for this SN subtype were not included in the original SNPhotCC library). Templates of subluminal SN 1991bg-like SNe Ia are also included. This library

of templates is not corrected for host extinction and is matched to the original LFs taken from L11. This approach of modelling the core-collapse SN population assumes that the reddening distribution in the data, the reddening distribution in the templates, and the reddening distribution in the sample of SNe used to measure the LFs are equal and representative.

A significant discrepancy is observed between the Hubble residual distribution measured from the SN data and that predicted from the simulations: a third of the SNe observed in the data with Hubble residuals in the range $0.5 < \mu_{\text{obs}} - \mu_{\text{model}} < 1.5$ mag are not present in the simulations. In J17, this is accounted for by adjusting the core-collapse LFs, brightening the L11 values by $\simeq 1$ mag, and fine-tuning the width of the LF (these adjusted LFs are also reported in Table 1). As discussed in J17, these adjustments are made after analysing the peak absolute brightnesses of the PS1 light curves

identified as SNe Ib/Ic or SNe II by the photometric classifier PSNID (Sako et al. 2011), after specific SALT2 cuts are applied to the sample, and are not necessarily representative of intrinsic SN LFs.

4.2.1 Implementation of the simulations

We repeat the J17 simulations of the PS1 photometric SN sample using our new template library to demonstrate its applicability to simulations of SN surveys. Our simulations use the same SNANA configuration files presented in J17, with the exception of revising the approach used to model and reproduce the core-collapse population. We test three alternative ways to generate core-collapse SNe:

- (i) using our uncorrected templates, matched with the revised L11 LFs (hereafter referred to as V19 + L11);
- (ii) using our host extinction-corrected templates matched with the R14 LFs, simulating additional host extinction ('V19 + R14 LFs');
- (iii) using our uncorrected templates, matched with the LFs adjusted by J17 ('V19 + J17').

For each approach, we generate 25 independent simulations, and our results for each case are then an average of these 25.

The method used to match the templates to the relative LF is straightforward. For each of the SN subtypes considered in our classification scheme, we compare the (biased) luminosity distribution measured from our set of templates to the corresponding LF. Subtype-dependent magnitude offsets and smearing factors are applied to the templates so that the peak brightnesses of simulated SN events have the correct distribution. By applying *subtype-dependent* magnitude offsets, we correct the overall brightness of each subclass of templates, thus retaining the relative brightness between individual templates of the same subtype. As a result, correlations intrinsic to subclasses of templates (e.g. faster declining SNe II are on average brighter than slower declining SNe II) are preserved in the simulations.

The relative rate of each template is calculated so that the core-collapse SN fractions presented in Shivvers et al. (2017) are correctly reproduced in the simulations. Within a subtype, each individual template is considered to be equally probable. For simulations using templates corrected for host galaxy extinction, the effect of host galaxy dust is simulated using the dust extinction distribution presented in Hatano, Branch & Deaton (1998) (see Appendix A).

We compare the results from these three approaches with the core-collapse contamination modelling adopted in J17 after the fine-tuning of the LFs (hereafter referred to as J17 templates with J17 adjusted LFs). This gives four families of simulations in total, three of which we run ourselves. The input files used to generate each simulation can be found in the package SNANA.

4.3 Results and discussion

We now turn to the results from our simulations. For each of the simulations, detected SNe are fitted using the SALT2.4 model (Guy et al. 2010), and the SALT2-based cuts of Betoule et al. (2014) and J17 are then applied. In J17, over 25 independent simulations, the average number of simulated SNe Ia passing SALT2-based cuts is 1021 ± 30 , which corresponds to 88.4 ± 3.7 per cent of the number of SNe observed in the PS1 sample after SALT2-based cuts ($1153 \text{ SNe} \pm \text{a Poisson error of } 34$). Assuming that simulations of SNe Ia

are correct and that each event in the data is either a SN Ia or a core-collapse SN, we expect to reproduce with simulations a fraction of core collapse of 11.6 ± 3.7 per cent.

In Fig. 8, we present for each simulation the predicted core-collapse contamination and the distribution of Hubble residuals. (In the discussion that follows, we remind the reader that the Hubble residual is defined as $\mu_{\text{obs}} - \mu_{\text{model}}$; i.e. brighter SNe have a negative Hubble residual.)

Comparing our results to the PS1 data, we observe the following:

(i) Simulations performed using revised L11 LFs and templates not corrected for host extinction (V19 + L11) predict a core-collapse contamination of 3.7 ± 0.5 per cent. The number of SNe in the fainter tail of the Hubble residuals is underestimated by a factor of approximately 2. This reproduces the result of J17 before the fine-tuning of the original L11 LFs, and shows that L11 LFs, used in either their original or revised form, underestimate the number of observed contaminants.

(ii) Simulations performed using R14 LFs and de-reddened templates not only underestimate the number of SNe in the fainter tail of the Hubble residuals but also overestimate the number of bright events (Hubble residuals with < -1 mag) by a factor of 3. The overall predicted contamination is 9.5 ± 0.9 per cent. The high fraction of bright events suggests that either the R14 LFs are over-represented in bright objects or the dust extinction applied in the simulations is underestimated (globally or for particular SN subtypes).

(iii) Simulations using the LFs adjusted by J17 (V19 + J17 and J17 simulations) better reproduce the overall Hubble residual distribution as expected, and predict a contamination of 7.5 ± 0.8 and 7.7 ± 0.9 per cent, respectively. However, we note that when our library of templates is used instead of the original J17 library, the agreement between the simulations and data slightly decreases. This suggests that LFs fine-tuned by J17 should be used with caution as they are fine-tuned to a specific set of core-collapse templates.

In Fig. 9, we compare simulated and observed Hubble residual distributions in different redshift bins ($z < 0.3$, $0.3 < z < 0.4$, and $z > 0.4$). We present separately the effects of the different LFs while fixing the template library (upper plot in Fig. 9) and then compare simulations implemented using the same LFs (J17 adjusted) but different template libraries (lower plot in Fig. 9). Different redshift ranges present different issues:

(i) At lower redshifts ($z < 0.3$), none of the simulations generated using our templates agree with the data. Despite the fact that the LFs tested are significantly different in terms of brightness (see Table 1), the number of SNe for Hubble residuals > 0.5 mag is systematically underpredicted by a factor of 2–3 (corresponding to 20–25 'missing' SNe). Even using de-reddened templates and simulating a range of dust extinctions (V19 + R14 set of simulations), we do not reproduce the observed contamination despite increasing significantly the colour diversity of the simulated light curves. At low redshifts, fainter SN events (e.g. stripped-envelope SNe or extincted SNe) are more likely to be detected; therefore, the diversity of the template library, the fraction of peculiar events included, and the extinction distribution assumed for each SN subtype all have a significant impact on the final results.

(ii) At higher redshift, the fraction of detected core-collapse SNe is reduced and the agreement between the data and simulations improves significantly. At $z > 0.4$, we note that the expected core-collapse fraction is larger than 12 per cent (with 366 ± 16 simulated SNe Ia in this redshift bin, and 417 observed SNe in the PS1 sample).

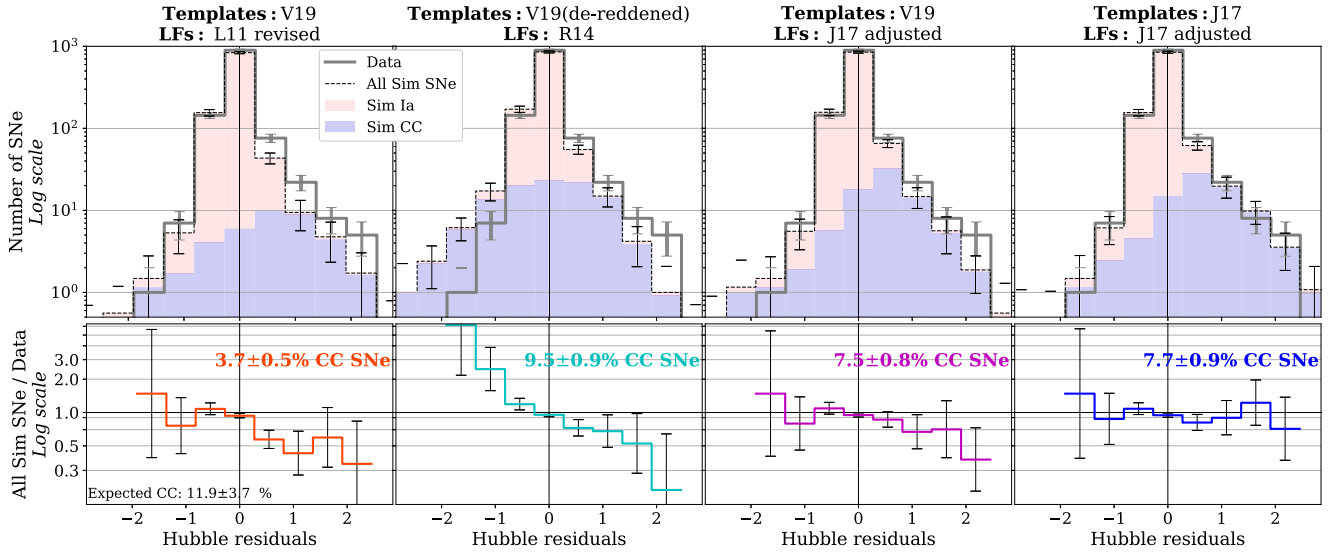


Figure 8. *Upper panels:* The Hubble residuals predicted (i) using our library of core-collapse templates generated without extinction corrections together with the revised **L11** LFs (left), (ii) using our library of extinction-corrected templates and the **R14** LFs (centre left), (iii) using our library of core-collapse templates generated without extinction corrections together with the LFs adjusted by **J17** (centre right), and (iv) using templates and LFs adopted in **J17**. Each panel shows the mean distribution of Hubble residuals averaged over 25 simulations. The distribution of Hubble residuals measured from all simulated SNe (core-collapse SNe and SNe Ia) is shown in black. Uncertainties are measured as the standard deviation over 25 simulations. The red and blue histograms show the stacked distributions of simulated SNe Ia and simulated core-collapse SNe, respectively. The distribution of Hubble residuals measured from the PS1 data and the relative Poisson errors are shown in grey. *Lower panels:* For each Hubble residual bin, we present the ratio of the number of all simulated SNe (SNe Ia and core-collapse SNe) and the number of actual observed SNe with the relative propagated uncertainties. The fraction of simulated core-collapse SNe over the total number of simulated SNe is indicated for each of the four simulations. The expected core-collapse contamination (assuming the number of simulated SNe Ia is correct and events in the data are either SNe Ia or core-collapse SNe) is also indicated. Except for simulations using LFs and templates from **J17**, the simulations are not in good agreement with the data for Hubble residuals larger than 0.5 mag.

This raises some concerns about the modelling of SNe Ia in this redshift bin. We note that simulations using the **R14** LFs can predict such a high contamination, but significantly overpredict the number of bright SNe (Hubble residuals of < -1 mag). Simulations using the **J17** LFs better reproduce the Hubble residuals in this redshift bin, but here we note that when our ‘near-UV extended’ templates are used, the predicted core-collapse contamination is two times larger than that produced with other templates. This suggests that the near-UV extension is important for simulations of core-collapse contamination at higher redshift.

Finally, Fig. 10 shows the contribution of each core-collapse SN type to the final simulated Hubble residual distributions. Several interesting trends emerge, highlighting the importance of the template library used in the simulations. For example, the number of SNe Ib and SNe Ic with Hubble residuals between -1 and $+1$ mag is larger for simulations in which the **R14** LFs and de-reddened templates are used. Two effects drive this result. First, a significant fraction of the SNe Ib and Ic entering our templates is highly reddened ($E(B - V) > 0.2$; see Fig. A4), and many simulated SNe Ib and Ic do not pass the SALT2 colour cuts if templates that include host extinction are used. Secondly, the **R14** LFs for SNe Ib and SNe Ic are brighter than those of **L11** or **J17**, even accounting for the differences in filters in which the two functions are constructed (B band versus R band).

We also note that more SNe IIn are detected in simulations using our templates, even when the same LF is used (third and fourth panels in Fig. 10). This is due to the larger diversity of SNe IIn captured in our library of templates, with both fast- and slow-declining SN IIn events included. In simulations where the **L11** revised LFs and **R14** LFs are used, a larger number of SNe IIn is

expected as the intrinsic brightness of SNe IIn is larger than that in the adjusted LFs of **J17** (see Table 1). Finally, we observe that the Hubble residual distribution of SNe II from simulations using our library of templates is shifted by approximately 0.5 mag when compared to simulations using the **J17** templates. This is true even when the same underlying LFs are used (third and fourth panels in Fig. 10) and is related to differences in the colour and stretch properties of the templates.

To conclude, analysing the Hubble residual distribution (globally, for different redshift bins and for different SN subtypes) is an important test for cosmological analyses. However, Hubble residuals are (by definition) conflated with SN parameters such as stretch and colour (equation 4), and various cuts based on these SN properties are also applied. Thus, the analysis of Hubble residuals alone cannot provide a fundamental understanding of whether it is the LFs, or the colour and stretch distributions and associated cuts, or both, that are driving the differences between observed and simulated samples. We leave for a future article a detailed comparison between various global properties of observed and simulated SNe, using the samples both before and after SN parameter-based cuts. However, understanding what drives the discrepancies between the data and simulations is crucial and provides important guidance in the design of realistic simulations of SNe of multiple types, essential to reduce systematic uncertainties due to core-collapse contamination in future SN Ia analyses.

5 SUMMARY AND FUTURE APPLICATIONS

We have presented a library of 67 spectral time-series templates of core-collapse SNe. Compared to existing core-collapse spectral

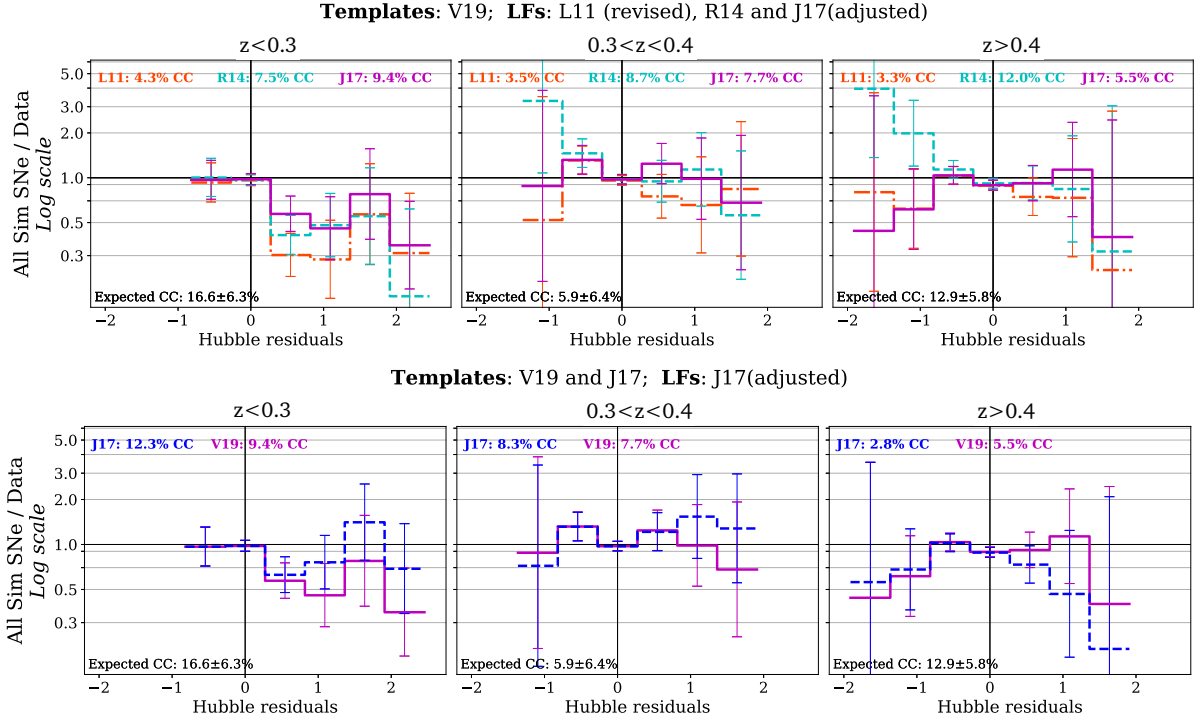


Figure 9. Ratio between the number of simulated SNe and number of observed SNe in each Hubble residual bin for three different redshift intervals: $z < 0.3$ (left, 368 SNe observed), $0.3 < z < 0.4$ (centre, 368 SNe observed), and $z > 0.4$ (right, 417 SNe observed). *Upper plot:* We compare the three simulations implemented using our library of templates, combined with three different LFs: revised L11 LFs (dash-dotted line), R14 LFs (dashed line), and J17 fine-tuned LFs (solid line). *Lower plot:* We compare the two simulations implemented using LFs fine-tuned by J17 and two different template libraries: the template library presented in this work (V19, solid line) and the J17 set of templates (dashed line). In every panel, the percentage of simulated core-collapse SNe over the total number of simulated SNe is shown for each simulation in each redshift bin. The expected core-collapse contamination (assuming the number of simulated SNe Ia is correct and events in the data are either SNe Ia or core-collapse SNe) is also indicated.

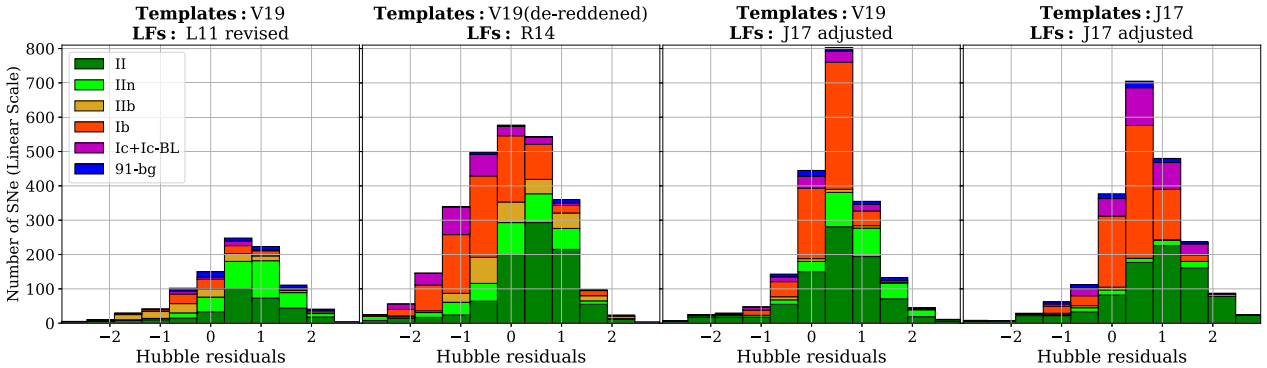


Figure 10. Stacked distributions of simulated Hubble residuals for different core-collapse SN types showing the relative importance of each SN type as a contaminant. The four panels show the results for the three simulations tested in this paper (Section 4.2.1) plus the J17 simulations. The results are the average of 25 different simulations.

models, our new set of templates represents a significant improvement in several ways. We highlight the following key features of our library:

- (i) Spectral templates included in the library are generated from multiband photometry and only sparsely sampled spectral data.
- (ii) Each template is generated from a single SN event, retaining the event-to-event diversity in the final library. No SED template or model is assumed, and the final daily sampled spectral time series for each SN is reconstructed in a fully data-driven fashion, with a heavy emphasis on GPs.

- (iii) Each template is extended in the near-UV to $\simeq 1600 \text{ \AA}$ using near-UV photometry. This is critical to simulate SN light curves at redshifts greater than 0.2.

- (iv) Each template has (optionally) been corrected for dust extinction in the SN host galaxy. As a result, different levels of host galaxy extinction, or different dust models, can be applied to the templates in simulations, and a realistic range of reddened SN light curves can be reproduced.

The techniques and code used to construct the spectral library are open source, and can, in principle, be applied to any type of transient

with well-constrained multiband photometry and spectroscopy. Given the large number of ongoing photometric and spectroscopic SN surveys, the number of SN events suitable for our method is likely to grow. This will boost our ability to improve and increase the diversity and size of core-collapse SN libraries, of key importance to future SN Ia cosmological studies.

As a demonstration of the spectral library, we used the core-collapse templates to simulate core-collapse contamination in photometrically selected SN Ia samples. We tested different core-collapse modelling approaches, exploiting the LFs and host extinction distributions currently available in the literature. Our analysis suggests that predictions from simulations are sensitive to how global core-collapse SN properties (such as luminosity, colour, and extinction distributions) are modelled. This suggests that, along with these improved libraries of core-collapse SN templates, it is critical to improve our knowledge of the global populations of core-collapse SN events.

ACKNOWLEDGEMENTS

We thank Rick Kessler and Dan Scolnic for their useful comments and feedback. This work was supported by the Science & Technology Facilities Council (STFC) (grant no. ST/P006760/1) through the DISCnet Centre for Doctoral Training. MS acknowledges funding from the STFC (grant no. ST/N002504/1) and from EU/FP7-ERC grant no. 615929. This work made use of WISEREP (<https://wiserep.weizmann.ac.il>) and the Open Supernova Catalog (<https://sne.space>). This research has made use of the CfA Supernova Archive, which is funded in part by the National Science Foundation through grant AST 0907903. This research made use of ASTROPY,⁶ a community-developed core Python package for astronomy (Astropy Collaboration 2013; Price-Whelan et al. 2018).

REFERENCES

- Ambikasaran S., Foreman-Mackey D., Greengard L., Hogg D. W., O’Neil M., 2015, *IEEE Trans. Pattern Anal. Mach. Intell.*, 38, 252
- Anderson J. P. et al., 2014, *ApJ*, 786, 67
- Anderson J. P. et al., 2018, *Nat. Astron.*, 2, 574
- Angus C. R., et al., 2019, *MNRAS*, 487, 2215
- Arcavi I. et al., 2011, *ApJ*, 742, L18
- Arcavi I. et al., 2012, *ApJ*, 756, L30
- Arcavi I. et al., 2017a, *Nature*, 551, 210
- Arcavi I. et al., 2017b, *ApJ*, 837, L2
- Astier P. et al., 2006, *A&A*, 447, 31
- Astropy Collaboration, 2013, *A&A*, 558, A33
- Azalee Bostroem K. et al., 2019, preprint ([arXiv:1901.09962](https://arxiv.org/abs/1901.09962))
- Barbary K. et al., 2016, *Astrophysics Source Code Library*, record ascl:1611.017
- Barbon R., Benetti S., Cappellaro E., Patat F., Turatto M., Iijima T., 1995, *A&AS*, 110, 513
- Barbon R., Benetti S., Cappellaro E., Rosino L., Turatto M., 1990, *A&A*, 237, 79
- Barbon R., Ciatti F., Rosino L., 1979, *A&A*, 72, 287
- Baron E., Branch D., Hauschildt P. H., 2007, *ApJ*, 662, 1148
- Bayless A. J. et al., 2013, *ApJ*, 764, L13
- Bazin G. et al., 2009, *A&A*, 499, 653
- Ben-Ami S. et al., 2012, *ApJ*, 760, L33
- Ben-Ami S. et al., 2015, *ApJ*, 803, 40
- Benetti S. et al., 2011, *MNRAS*, 411, 2726
- Bersten M. C. et al., 2018, *Nature*, 554, 497
- Betoule M. et al., 2014, *A&A*, 568, A22
- Bianco F. B. et al., 2014, *ApJS*, 213, 19
- Black C. S., Milisavljevic D., Margutti R., Fesen R. A., Patnaude D., Parker S., 2017, *ApJ*, 848, 5
- Bose S., Kumar B., Misra K., Matsumoto K., Kumar B., Singh M., Fukushima D., Kawabata M., 2016, *MNRAS*, 455, 2712
- Bose S. et al., 2013, *MNRAS*, 433, 1871
- Bose S. et al., 2015a, *MNRAS*, 450, 2373
- Bose S. et al., 2015b, *ApJ*, 806, 160
- Brown P. J., Breeveld A., Roming P. W. A., Siegel M., 2016, *AJ*, 152, 102
- Brown P. J., Breeveld A., Holland S., Kuin P., Pritchard T., 2014, *Ap&SS*, 354, 89
- Brown P. J., Roming P. W. A., Milne P. A., 2015, *J. High Energy Astrophys.*, 7, 111
- Bufano F. et al., 2009, *ApJ*, 700, 1456
- Bufano F. et al., 2014, *MNRAS*, 439, 1807
- Bullivant C. et al., 2018, *MNRAS*, 476, 1497
- Buton C. et al., 2013, *A&A*, 549, A8
- Campbell H. et al., 2013, *ApJ*, 763, 88
- Cao Y. et al., 2013, *ApJ*, 775, L7
- Cardelli J. A., Clayton G. C., Mathis J. S., 1989, *ApJ*, 345, 245
- Catchpole R. M. et al., 1987, *MNRAS*, 229, 15P
- Catchpole R. M. et al., 1988, *MNRAS*, 231, 75p
- Catchpole R. M. et al., 1989, *MNRAS*, 237, 55P
- Chen J. et al., 2014, *ApJ*, 790, 120
- Childress M. J. et al., 2016, *Publ. Astron. Soc. Aust.*, 33, e055
- Chornock R. et al., 2013, *ApJ*, 767, 162
- Chugai N. N., 1990, *Sov. Astron. Lett.*, 16, 457
- Clocchiatti A., Wheeler J. C., Brotherton M. S., Cochran A. L., Wills D., Barker E. S., Turatto M., 1996, *ApJ*, 462, 462
- Conley A. et al., 2008, *ApJ*, 681, 482
- Dall’Ora M. et al., 2014, *ApJ*, 787, 139
- Dhungana G. et al., 2016, *ApJ*, 822, 6
- Drout M. R. et al., 2011, *ApJ*, 741, 97
- Drout M. R. et al., 2016, *ApJ*, 821, 57
- Elias-Rosa N. et al., 2010, *ApJ*, 714, L254
- Ergon M. et al., 2014, *A&A*, 562, A17
- Faran T. et al., 2014a, *MNRAS*, 442, 844
- Faran T. et al., 2014b, *MNRAS*, 445, 554
- Feroz F., Hobson M. P., 2008, *MNRAS*, 384, 449
- Feroz F., Hobson M. P., Bridges M., 2009, *MNRAS*, 398, 1601
- Filippenko A. V., 1997, *ARA&A*, 35, 309
- Filippenko A. V., Matheson T., Ho L. C., 1993, *ApJ*, 415, L103
- Filippenko A. V. et al., 1995, *ApJ*, 450, L11
- Folatelli G. et al., 2006, *ApJ*, 641, 1039
- Foley R. J. et al., 2003, *PASP*, 115, 1220
- Fraser M. et al., 2013, *MNRAS*, 433, 1312
- Fremling C. et al., 2014, *A&A*, 565, A114
- Fremling C. et al., 2016, *A&A*, 593, A68
- Gal-Yam A., 2017, in Alsabti A. W., Murdin P., eds, *Handbook of Supernovae*. Springer-Verlag, Berlin
- Gal-Yam A., Ofek E. O., Shemmer O., 2002, *MNRAS*, 332, L73
- Gal-Yam A. et al., 2008, *ApJ*, 685, L117
- Galama T. J. et al., 1998, *Nature*, 395, 670
- Galbany L. et al., 2016, *AJ*, 151, 33
- Gong Y., Cooray A., Chen X., 2010, *ApJ*, 709, 1420
- González-Gaitán S. et al., 2015, *MNRAS*, 451, 2212
- Graham M. L. et al., 2014, *ApJ*, 787, 163
- Guillochon J., Parrent J., Kelley L. Z., Margutti R., 2017, *ApJ*, 835, 64
- Gutiérrez C. P. et al., 2017a, *ApJ*, 850, 89
- Gutiérrez C. P. et al., 2017b, *ApJ*, 850, 90
- Guy J. et al., 2007, *A&A*, 466, 11
- Guy J. et al., 2010, *A&A*, 523, A7
- Hamuy M. et al., 2001, *ApJ*, 558, 615
- Harutyunyan A. H. et al., 2008, *A&A*, 488, 383
- Hatano K., Branch D., Deaton J., 1998, *ApJ*, 502, 177
- Hicken M. et al., 2017, *ApJS*, 233, 6
- Hlozek R. et al., 2012, *ApJ*, 752, 79

⁶<http://www.astropy.org>

- Hosseinzadeh G. et al., 2018, *ApJ*, 861, 63
- Hsiao E. Y., Conley A., Howell D. A., Sullivan M., Pritchett C. J., Carlberg R. G., Nugent P. E., Phillips M. M., 2007, *ApJ*, 663, 1187
- Huang F. et al., 2018, *MNRAS*, 475, 3959
- Humphreys R. M., Davidson K., Jones T. J., Pogge R. W., Grammer S. H., Prieto J. L., Pritchard T. A., 2012, *ApJ*, 760, 93
- Hunter D. J. et al., 2009, *A&A*, 508, 371
- Inserra C., Prats S., Gutierrez C. P., Angus C., Smith M., Sullivan M., 2018, *ApJ*, 854, 175
- Inserra C. et al., 2011, *MNRAS*, 417, 261
- Inserra C. et al., 2012, *MNRAS*, 422, 1122
- Inserra C. et al., 2013, *A&A*, 555, A142
- Ishida E. E. O., de Souza R. S., 2013, *MNRAS*, 430, 509
- Izzo L. et al., 2019, *Nature*, 565, 324
- Jones D. O. et al., 2017, *ApJ*, 843, 6 (J17)
- Jones D. O. et al., 2018, *ApJ*, 857, 51
- Karpenka N. V., Feroz F., Hobson M. P., 2013, *MNRAS*, 429, 1278
- Kessler R., Conley A., Jha S., Kuhlmann S., 2010a, preprint (arXiv:1001.5210)
- Kessler R., Scolnic D., 2017, *ApJ*, 836, 56
- Kessler R. et al., 2009, *PASP*, 121, 1028
- Kessler R. et al., 2010b, *PASP*, 122, 1415
- Khazov D. et al., 2016, *ApJ*, 818, 3
- Kim A. G. et al., 2013, *ApJ*, 766, 84
- Krisciunas K. et al., 2009, *AJ*, 137, 34
- Kumar B. et al., 2013, *MNRAS*, 431, 308
- Kunz M., Bassett B. A., Hlozek R. A., 2007, *Phys. Rev. D*, 75, 103508
- Kuznetsova N. V., Connolly B. M., 2007, *ApJ*, 659, 530
- Landolt A. U., 1992, *AJ*, 104, 340
- Leaman J., Li W., Chornock R., Filippenko A. V., 2011, *MNRAS*, 412, 1419
- Leibundgut B., Tammann G. A., Cadonau R., Cerrito D., 1991, *A&AS*, 89, 537
- Leonard D. C. et al., 2002, *PASP*, 114, 35
- Li W., Filippenko A. V., Chornock R., Jha S., 2003, *PASP*, 115, 844
- Li W. et al., 2011, *MNRAS*, 412, 1441 (L11)
- Lochner M., McEwen J. D., Peiris H. V., Lahav O., Winter M. K., 2016, *ApJS*, 225, 31
- Maguire K. et al., 2010, *MNRAS*, 404, 981
- Margutti R. et al., 2014, *ApJ*, 780, 21
- Markwardt C. B., 2009, in Bohlender D. A., Durand D., Dowler P., eds, ASP Conf. Ser. Vol. 411, Astronomical Data Analysis Software and Systems XVIII. Astron. Soc. Pac., San Francisco, p. 251
- Matheson T., Filippenko A. V., Ho L. C., Barth A. J., Leonard D. C., 2000b, *AJ*, 120, 1499
- Matheson T. et al., 2000a, *AJ*, 120, 1487
- Mauerhan J. C. et al., 2013a, *MNRAS*, 430, 1801
- Mauerhan J. C. et al., 2013b, *MNRAS*, 431, 2599
- Mazzali P. A. et al., 2008, *Science*, 321, 1185
- Meza N. et al., 2019, *A&A*, 629, A57
- Milislavljevic D., Fesen R., Nordsieck K., Pickering T., Gulbis A., O'Donoghue D., 2011, Cent. Bur. Electron. Telegrams, 2777, 3
- Milislavljevic D. et al., 2013a, *ApJ*, 767, 71
- Milislavljevic D. et al., 2013b, *ApJ*, 770, L38
- Milislavljevic D. et al., 2015, *ApJ*, 799, 51
- Modjaz M., Kirshner R. P., Blondin S., Challis P., Matheson T., 2008, *ApJ*, 687, L9
- Modjaz M. et al., 2006, *ApJ*, 645, L21
- Modjaz M. et al., 2009, *ApJ*, 702, 226
- Modjaz M. et al., 2014, *AJ*, 147, 99
- Morales-Garoffolo A. et al., 2014, *MNRAS*, 445, 1647
- Morales-Garoffolo A. et al., 2015, *MNRAS*, 454, 95
- Munari U., Henden A., Belligoli R., Castellani F., Cherini G., Righetti G. L., Vagnozzi A., 2013, *New Astron.*, 20, 30
- Möller A., de Boissière T., 2019, preprint (arXiv:1901.06384)
- Nakaoka T. et al., 2018, *ApJ*, 859, 78
- Nugent P., Kim A., Perlmutter S., 2002, *PASP*, 114, 803
- Pandey S. B., Anupama G. C., Sagar R., Bhattacharya D., Sahu D. K., Pandey J. C., 2003, *MNRAS*, 340, 375
- Pastorello A. et al., 2006, *MNRAS*, 370, 1752
- Pastorello A. et al., 2008, *MNRAS*, 389, 955
- Pastorello A. et al., 2009, *MNRAS*, 394, 2266
- Pastorello A. et al., 2015, *MNRAS*, 449, 1921
- Patat F., Barbon R., Cappellaro E., Turatto M., 1994, *A&A*, 282, 731
- Patat F. et al., 2001, *ApJ*, 555, 900
- Perets H. B. et al., 2010, *Nature*, 465, 322
- Perlmutter S. et al., 1999, *ApJ*, 517, 565
- Pian E. et al., 2006, *Nature*, 442, 1011
- Pignata G. et al., 2009, Cent. Bur. Electron. Telegrams, 1731, 1
- Pignata G. et al., 2011, *ApJ*, 728, 14
- Piro A. L., Nakar E., 2013, *ApJ*, 769, 67
- Poznanski D., Prochaska J. X., Bloom J. S., 2012, *MNRAS*, 426, 1465
- Prentice S. J. et al., 2016, *MNRAS*, 458, 2973
- Price-Whelan A. M. et al., 2018, *AJ*, 156, 123
- Pritchard T. A., Roming P. W. A., Brown P. J., Bayless A. J., Frey L. H., 2014, *ApJ*, 787, 157
- Pun C. S. J. et al., 1995, *ApJS*, 99, 223
- Rasmussen C. E., 2006, Gaussian Processes for Machine Learning. MIT Press, Cambridge, MA
- Rest A. et al., 2014, *ApJ*, 795, 44
- Richardson D., Branch D., Casebeer D., Millard J., Thomas R. C., Baron E., 2002, *AJ*, 123, 745
- Richardson D., Jenkins R. L., III, Wright J., Maddox L., 2014, *AJ*, 147, 118 (R14)
- Richmond M. W., 2014, J. Am. Assoc. Var. Star Obs., 42, 333
- Richmond M. W., Treffers R. R., Filippenko A. V., Paik Y., Leibundgut B., Schulman E., Cox C. V., 1994, *AJ*, 107, 1022
- Richmond M. W. et al., 1996, *AJ*, 111, 327
- Riess A. G. et al., 1998, *AJ*, 116, 1009
- Rodney S. A., Tonry J. L., 2009, *ApJ*, 707, 1064
- Roming P. W. A. et al., 2005, *Space Sci. Rev.*, 120, 95
- Roming P. W. A. et al., 2012, *ApJ*, 751, 92
- Roy R. et al., 2011, *ApJ*, 736, 76
- Roy R. et al., 2013, *MNRAS*, 434, 2032
- Rubin A. et al., 2016, *ApJ*, 820, 33
- Sahu D. K., Anupama G. C., Chakradhari N. K., 2013, *MNRAS*, 433, 2
- Sahu D. K., Anupama G. C., Srividya S., Muneer S., 2006, *MNRAS*, 372, 1315
- Sahu D. K., Tanaka M., Anupama G. C., Gurugubelli U. K., Nomoto K., 2009, *ApJ*, 697, 676
- Sako M. et al., 2008, *AJ*, 135, 348
- Sako M. et al., 2011, *ApJ*, 738, 162
- Sanders N. E. et al., 2015, *ApJ*, 799, 208
- Saunders C. et al., 2018, *ApJ*, 869, 167
- Savitzky A., Golay M. J. E., 1964, Anal. Chem., 36, 1627
- Schlegel D. J., Finkbeiner D. P., Davis M., 1998, *ApJ*, 500, 525
- Schlegel E. M., 1990, *MNRAS*, 244, 269
- Scolnic D., Kessler R., 2016, *ApJ*, 822, L35
- Scolnic D. M. et al., 2018, *ApJ*, 859, 101
- Shivvers I. et al., 2016, *MNRAS*, 461, 3057
- Shivvers I. et al., 2017, *PASP*, 129, 054201
- Shivvers I. et al., 2019, *MNRAS*, 482, 1545
- Silverman J. M. et al., 2012, *MNRAS*, 425, 1789
- Silverman J. M. et al., 2017, *MNRAS*, 467, 369
- Smart S. J. et al., 2015, *A&A*, 579, A40
- Smith N., Chornock R., Li W., Ganeshalingam M., Silverman J. M., Foley R. J., Filippenko A. V., Barth A. J., 2008, *ApJ*, 686, 467
- Sonbas E. et al., 2008, *Astrophys. Bull.*, 63, 228
- Srivastav S., Anupama G. C., Sahu D. K., 2014, *MNRAS*, 445, 1932
- Stritzinger M. D. et al., 2018a, *A&A*, 609, A134
- Stritzinger M. D. et al., 2018b, *A&A*, 609, A135
- Stritzinger M. et al., 2009, *ApJ*, 696, 713
- Taddia F. et al., 2013, *A&A*, 555, A10
- Taddia F. et al., 2015, *A&A*, 574, A60
- Taddia F. et al., 2018, *A&A*, 609, A136
- Takaki K. et al., 2013, *ApJ*, 772, L17
- Takáts K. et al., 2014, *MNRAS*, 438, 368

- Takáts K. et al., 2015, *MNRAS*, 450, 3137
 Tartaglia L. et al., 2017, *ApJ*, 836, L12
 Taubenberger S. et al., 2006, *MNRAS*, 371, 1459
 Taubenberger S. et al., 2009, *MNRAS*, 397, 677
 Taubenberger S. et al., 2011, *MNRAS*, 413, 2140
 Terreran G. et al., 2016, *MNRAS*, 462, 137
 Terreran G. et al., 2017, *Nat. Astron.*, 1, 713
 The PLAsTiCC team et al., 2018, preprint (arXiv:1810.00001)
 Tomasella L. et al., 2013, *MNRAS*, 434, 1636
 Tripp R., 1998, *A&A*, 331, 815
 Tsvetkov D. Y., et al., 2012, *Peremennye Zvezdy (Variable Stars)*, 32, 6
 Turatto M., Benetti S., Cappellaro E., 2003, in Hillebrandt W., Leibundgut B., eds, *From Twilight to Highlight: The Physics of Supernovae*. Springer, Berlin, p. 200
 Vacca W. D., Leibundgut B., 1996, *ApJ*, 471, L37
 Valenti S. et al., 2008, *ApJ*, 673, L155
 Valenti S. et al., 2011, *MNRAS*, 416, 3138
 Valenti S. et al., 2012, *ApJ*, 749, L28
 Valenti S. et al., 2014, *MNRAS*, 438, L101
 Valenti S. et al., 2015, *MNRAS*, 448, 2608
 Valenti S. et al., 2016, *MNRAS*, 459, 3939
 Van Dyk S. D. et al., 2014, *AJ*, 147, 37
 Walker A. R., Suntzeff N. B., 1990, *PASP*, 102, 131
 Whitelock P. A. et al., 1988, *MNRAS*, 234, 5P
 Yaron O., Gal-Yam A., 2012, *PASP*, 124, 668
 Yaron O. et al., 2017, *Nat. Phys.*, 13, 510
 Yuan F. et al., 2016, *MNRAS*, 461, 2003
 Zhang J. et al., 2014, *ApJ*, 797, 5
 Zwitter T., Munari U., Moretti S., 2004, *IAU Circ.*, 8413

SUPPORTING INFORMATION

Supplementary data are available at *MNRAS* online.

Figure 2. Fit of multiband light curves using GPs for the SN Ib iPTF13bvn.

Figure 6. Synthetic multiband photometry estimated using the SN template built from the SN Ib iPTF13bvn.

Please note: Oxford University Press is not responsible for the content or functionality of any supporting materials supplied by the authors. Any queries (other than missing material) should be directed to the corresponding author for the article.

APPENDIX A: HOST GALAXY EXTINCTION ESTIMATES AND DISTRIBUTIONS

A1 Host galaxy extinction corrections

Estimating the extinction on SNe due to dust in the SN host galaxy is challenging. While extinction due to dust in the Milky Way is straightforward to estimate using published galactic dust maps, measuring extinction for SNe located in other galaxies requires more indirect techniques and often relies on empirically derived relations. Despite the large uncertainties – and indeed possible biases – associated with such host extinction corrections, we still choose to provide host extinction-corrected templates as an option for the end user. Several SNe included in our library are highly reddened events, and using these templates in simulations without extinction corrections may not be useful (or at least potentially misleading). In this appendix, we describe our approach and implementation to extinction corrections.

For most (63 out of 67) of the SNe considered in this paper, we have found a published estimate of the host galaxy reddening, and we therefore apply extinction corrections based on these estimates

to provide templates that are corrected for dust at least to first order. These estimates are reported in Table 2 as the colour excess due to host galaxy dust, $E(B - V)_{\text{host}}$.

Most of these estimates of $E(B - V)_{\text{host}}$ have been estimated using the equivalent width of the NaID absorption lines, and applying the empirically derived relation presented in Turatto et al. (2003). However, this method presents a large scatter and generally requires high-resolution spectroscopy (Barbon et al. 1990; Poznanski, Prochaska & Bloom 2012; Stritzinger et al. 2018b). An alternative is to use the colour evolution of SNe by comparing the colour evolution of a SN to either intrinsic colour templates (Drout et al. 2011; Taddia et al. 2015) or samples of SNe thought to suffer minimal extinction (Stritzinger et al. 2018b). This approach is popular in studies of stripped-envelope SNe that preferentially occur in regions of high star formation where extinction can be higher and thus more important to correct for. When extinction estimates from this approach are available, we use these in preference to those based on NaID absorption. For SNe that present negligible reddening (<0.01 mag), we set $E(B - V)_{\text{host}}$ to zero. For SNe that lack any information about host reddening (4 out of 67 SNe), we use the average $E(B - V)_{\text{host}}$ estimated by Prentice et al. (2016).

In Figs A1 and A2, we show the synthetic $B - V$, $V - R$, and $uvwI - V$ colour evolution measured from our templates both before and after our host extinction corrections. For both stripped-envelope SNe and hydrogen-rich SNe, the scatter in colour at fixed phase is reduced after extinction corrections are applied, with the mean $B - V$ colour decreased by 0.1–0.15 mag.

We compare these findings with previous analyses. Drout et al. (2011) estimated the scatter in $(V - R)$ at 10 d after V-band maximum (σ_{V-R}) for a sample of 10 well-observed stripped-envelope SNe (8 are included in our library), and find $\sigma_{V-R} = 0.06$ mag. We measure $\sigma_{V-R} = 0.12$ mag for our 37 stripped-envelope SNe (reducing to 0.07 when only the 8 SNe included in Drout et al. (2011) analysis are considered). If we compare the scatter of $(B - V)$ at 10 d after V-band maximum measured from our stripped-envelope SN templates with the sample of minimally reddened stripped-envelope SNe in Stritzinger et al. (2018b) (Table 2), the scatter in our templates is around a factor of 2 or more larger. These discrepancies are likely due to limitations in the host extinction corrections, but also due to the larger diversity included in our templates.

A1.1 Consequences of incorrect host extinction corrections in the near-UV

Figs A1 and A2 suggest that extinction corrections reduce the scatter in the colour of SN templates within the same class. However, some important caveats related to dust extinction corrections need to be highlighted.

Stritzinger et al. (2018b) suggest that SNe Ic preferentially occur in dust regions characterized by a larger value of R_V^{host} . Trends like this are more important for our study than the accuracy of an individual host extinction estimate, particularly in the colour of the templates and particularly in the near-UV. In Fig. A3, we show how the extinction changes in the near-UV relative to the optical for different $E(B - V)$ and R_V . Assuming that the correct value of $E(B - V)_{\text{host}}$ is known, extinction corrections that assume smaller values of R_V^{host} than the sample average will underpredict the amount of extinction in the near-UV. One consequence of this, from the perspective of using these templates for simulating contamination in SNe Ia cosmological analyses, would be an

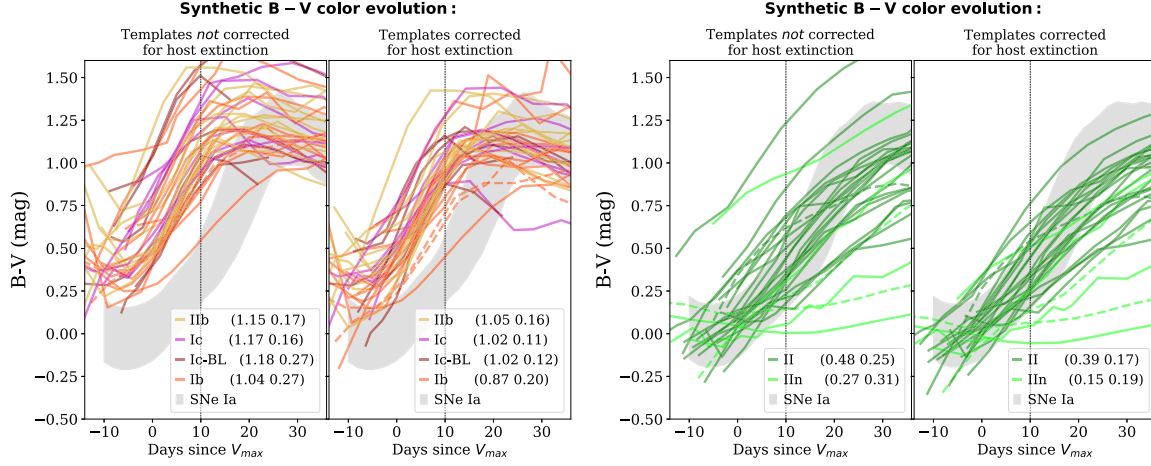


Figure A1. *Left figure:* Time evolution of the $B - V$ colour synthesized from our stripped-envelope SN templates before host extinction corrections (left-hand panel) and after host extinction corrections (right-hand panel). The average $B - V$ scatter at 10 d after V -band maximum and the relative standard deviation are shown in the legend. For comparison, we also show the $B - V$ colour evolution of SNe Ia (grey area) generated using SN Ia light curves with SALT2 stretch and colour parameters randomly distributed between $-3 < x_1 < 3$ and $-0.3 < C < 0.3$. Dashed lines indicate SNe that have been corrected using the average host extinction presented in Prentice et al. (2016). *Right figure:* Same as the left figure, but for the hydrogen-rich SN templates.

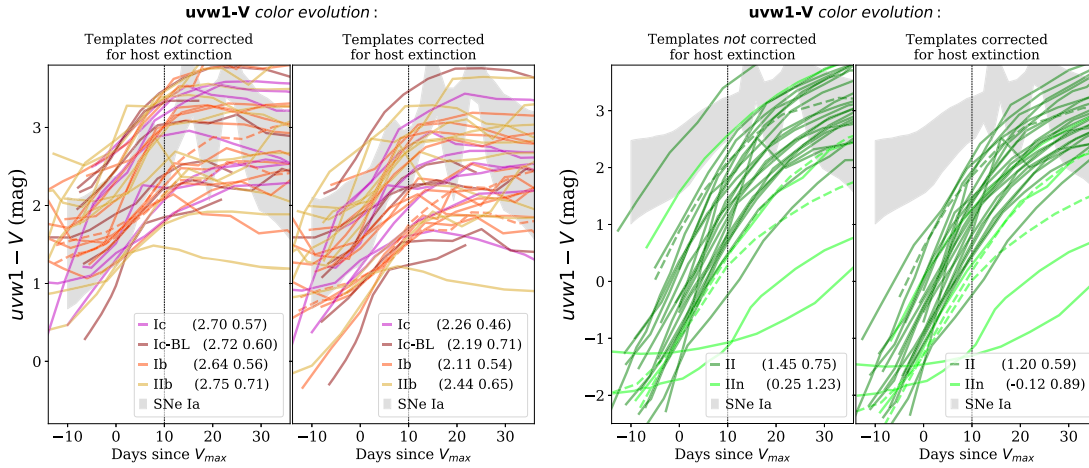


Figure A2. Same as Fig. A1, but for the $uvw1 - V$ colour.

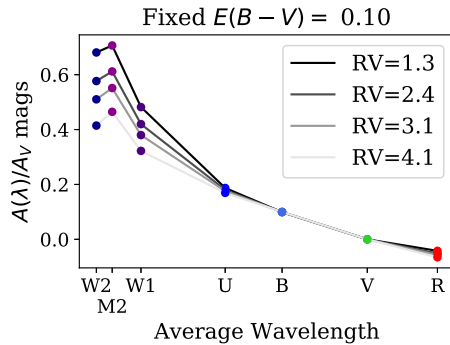


Figure A3. Extinction correction in optical and UV filters for different values of $E(B - V)$ ($E(B - V) = 0.05$ on the left, $E(B - V) = 0.1$ in the centre, and $E(B - V) = 0.25$ on the right) and for different values of R_V . The Cardelli et al. (1989) dust law is assumed.

overestimate/underestimate of the SN Ic contamination at higher redshift where the rest-frame near-UV is redshifted into the optical. For this reason, we tested colour corrections applying the set of R_V^{host} as suggested in Stritzinger et al. (2018b) for different types of stripped-envelope SNe: $R_V^{\text{host}} = 1.1$ for SNe Iib, $R_V^{\text{host}} = 2.6$ for SNe Ib, and $R_V^{\text{host}} = 4.3$ for SNe Ic. However, we do not observe any reduction in the scatter in the colour evolution of the templates.

A2 Distribution of host galaxy extinction compared with the literature

In Table 2, we summarize the values of Milky Way and host galaxy reddening assumed in this work. We compare the distribution of host galaxy extinction observed in our sample with the results presented in Prentice et al. (2016) and Hatano et al. (1998). Both studies estimate the distribution of host galaxy extinction for core-collapse SNe, the first from a data-driven perspective and the second using simulations.

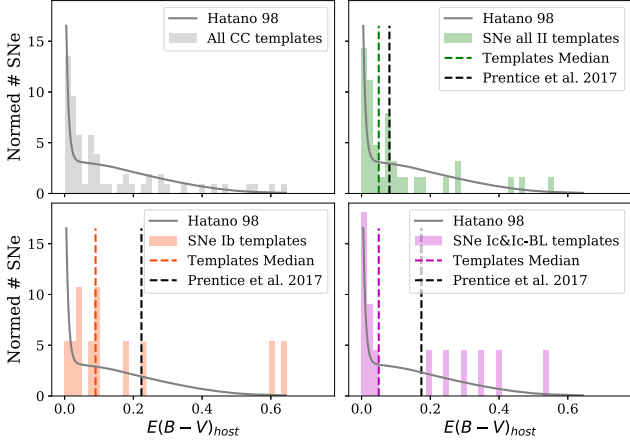


Figure A4. Normalized distribution of host galaxy reddening in our sample of core-collapse SNe. We show the results for all core-collapse SNe (upper left), for SNe IIb, IIc, and II (upper right), for SNe Ib (lower left), and for SNe Ic/Ic-BL (lower right). In each panel, the median host extinction measured from our sample of SNe and that from Prentice et al. (2016) are shown. The normalized distribution of host reddening predicted from Hatano et al. (1998), and approximated by summing an exponential and Gaussian distribution, is also shown (solid grey line).

Prentice et al. (2016) analysed a sample of 110 core-collapse SNe with well-constrained host galaxy extinction estimates, and measured the mean and median reddening observed for SNe Ib, Ic/Ic-BL, and II (including SNe IIb and IIc) separately. On average, SNe Ib and Ic/Ic-BL are (respectively) three and two times more extinguished than hydrogen-rich core-collapse SNe, suggesting differences in the properties of the environments where these events occur.

A different approach was taken by Hatano et al. (1998), who used Monte Carlo techniques to estimate the extinction distribution

expected given a set of randomly inclined spiral galaxies, applying some basic modelling of how dust and the progenitors of SNe are spatially distributed in galaxies. They neglected any differences in the spatial distribution of different core-collapse SN subtypes. The distribution of V -band extinction found by Hatano et al. (1998)⁷ can be approximated with the following expression:

$$f(A_V)dA_V = e^{-0.016A_V} + 0.080\mathcal{N}(0, 0.801).$$

This approximate distribution can be implemented in SNANA, and used to simulate the host galaxy extinction of core-collapse SNe.

These two studies are complementary: the first reveals the subtype dependence of the host extinction distribution, while the second provides an unbiased estimate of the host extinction distribution for core-collapse SNe of all subtypes. In Fig. A4, we show the distribution of $E(B - V)$ measured for our set of templates and compare it with the results presented in Prentice et al. (2016) and Hatano et al. (1998). The upper left panel of Fig. A4 shows that the distribution observed in the data is in overall agreement with the predictions from Hatano et al. (1998).

We note the fact that SNe Ib and Ic/Ic-BL present larger tails of highly reddened objects compared to SNe II, which suggests that different host extinction distributions should perhaps be used for different core-collapse subtypes. However, the median extinction

⁷Hatano et al. (1998) present the distribution of B -band extinction, $f(A_B)dA_B$. This can be converted to $f(A_V)dA_V$ assuming the relation $A_V = (3.1/4.1) \cdot A_B$. values measured from our sample of SNe Ib and Ic/Ic-BL are, respectively, a factor of 2 and a factor of 4 lower than that in Prentice et al. (2016). This suggests that different biases affect the samples considered, with our sample likely excluding some highly extinguished objects.

This paper has been typeset from a \LaTeX file prepared by the author.